



## RESEARCH ARTICLE

10.1029/2017JD027818

## Key Points:

- Even at 590-nm wavelength, brC in the exhaust of an engine operated on heavy fuel oil (HFO) was responsible for 20% of total PM absorption
- HFO contains very large rBC particles (mode at 640-nm volume-equivalent diameter)
- We report wavelength-dependent imaginary refractive indices and mass absorption cross sections for brown carbon

## Supporting Information:

- Supporting Information S1

## Correspondence to:

J. C. Corbin and M. Gysel,  
Joel.Corbin@nrc-cnrc.gc.ca;  
martin.gysel@psi.ch

## Citation:

Corbin, J. C., Pieber, S. M., Czech, H., Zanatta, M., Jakobi, G., Massabò, D., et al. (2018). Brown and black carbon emitted by a marine engine operated on heavy fuel oil and distillate fuels: Optical properties, size distributions, and emission factors. *Journal of Geophysical Research: Atmospheres*, 123, 6175–6195. <https://doi.org/10.1029/2017JD027818>

Received 1 NOV 2017

Accepted 1 MAY 2018

Accepted article online 11 MAY 2018

Published online 15 JUN 2018

©2018. The Authors.

This is an open access article under the terms of the Creative Commons Attribution-NonCommercial-NoDerivs License, which permits use and distribution in any medium, provided the original work is properly cited, the use is non-commercial and no modifications or adaptations are made.

# Brown and Black Carbon Emitted by a Marine Engine Operated on Heavy Fuel Oil and Distillate Fuels: Optical Properties, Size Distributions, and Emission Factors

J. C. Corbin<sup>1,2</sup> , S. M. Pieber<sup>1</sup> , H. Czech<sup>3</sup> , M. Zanatta<sup>1,4</sup>, G. Jakobi<sup>5,6</sup>, D. Massabò<sup>7,8</sup> , J. Orasche<sup>3,5,6</sup>, I. El Haddad<sup>1</sup>, A. A. Mensah<sup>9</sup> , B. Stengel<sup>6,10</sup>, L. Drinovec<sup>11,12</sup> , G. Mocnik<sup>11,12</sup> , R. Zimmermann<sup>3,5,6</sup>, A. S. H. Prévôt<sup>1</sup>, and M. Gysel<sup>1</sup>

<sup>1</sup>Laboratory of Atmospheric Chemistry, Paul Scherrer Institute, Villigen, Switzerland, <sup>2</sup>Now at National Research Council Canada, Ottawa, Canada, <sup>3</sup>Joint Mass Spectrometry Centre, Chair of Analytical Chemistry, Institute of Chemistry, University of Rostock, Rostock, Germany, <sup>4</sup>Now at Alfred Wegener Institute, Bremerhaven, Germany, <sup>5</sup>Joint Mass Spectrometry Centre, Cooperation Group Comprehensive Molecular Analytics, Helmholtz Zentrum München, Neuherberg, Germany, <sup>6</sup>Helmholtz Virtual Institute for Complex Molecular Systems in Environmental Health, Neuherberg, Germany, <sup>7</sup>Department of Physics, University of Genoa, Genova, Italy, <sup>8</sup>INFN, Sezione di Genova, Genova, Italy, <sup>9</sup>Institute for Atmospheric and Climate Science, ETH Zurich, Zurich, Switzerland, <sup>10</sup>Department of Piston Machines and Internal Combustion Engines, University of Rostock, Rostock, Germany, <sup>11</sup>Aerosol d.o.o., Ljubljana, Slovenia, <sup>12</sup>Now at Condensed Matter Physics Department, Jožef Stefan Institute, Ljubljana, Slovenia

**Abstract** We characterized the chemical composition and optical properties of particulate matter (PM) emitted by a marine diesel engine operated on heavy fuel oil (HFO), marine gas oil (MGO), and diesel fuel (DF). For all three fuels, ~80% of submicron PM was organic (and sulfate, for HFO at higher engine loads). Emission factors varied only slightly with engine load. Refractory black carbon (rBC) particles were not thickly coated for any fuel; rBC was therefore externally mixed from organic and sulfate PM. For MGO and DF PM, rBC particles were lognormally distributed in size (mode at  $d_{rBC} \approx 120$  nm). For HFO, much larger rBC particles were present. Combining the rBC mass concentrations with in situ absorption measurements yielded an rBC mass absorption coefficient  $MAC_{BC,780\text{nm}}$  of  $7.8 \pm 1.8$  m<sup>2</sup>/g at 780 nm for all three fuels. Using positive deviations of the absorption Ångström exponent (AAE) from unity to define brown carbon (brC), we found that brC absorption was negligible for MGO or DF PM ( $AAE(370,880\text{nm}) \approx 1.0 \pm 0.1$ ) but typically 50% of total 370-nm absorption for HFO PM. Even at 590 nm, ~20% of the total absorption was due to brC. Using absorption at 880 nm as a reference for BC absorption and normalizing to organic PM mass, we obtained a  $MAC_{OM,370\text{nm}}$  of 0.4 m<sup>2</sup>/g at typical operating conditions. Furthermore, we calculated an imaginary refractive index of  $(0.045 \pm 0.025)(\lambda/370\text{nm})^{-3}$  for HFO PM at  $370\text{nm} < \lambda < 660\text{nm}$ , more than twofold greater than previous recommendations. Climate models should account for this substantial brC absorption in HFO PM.

**Plain Language Summary** We characterized the fundamental properties of marine engine exhaust that are relevant to its aerosol-radiation interactions in climate models. In particular, we focussed on “brown carbon” light absorption (i.e., absorption in excess of that expected for the black carbon in canonical soot). We found that brown carbon can increase the direct radiative forcing of heavy-fuel-oil ship exhaust by 18% over snow.

## 1. Introduction

Ship engines are the major source of combustion aerosols in the marine environment, where almost no other anthropogenic pollution sources exist. Understanding the climate-relevant optical properties of this particulate matter (PM) is therefore essential to the accurate determination of anthropogenic radiative effects on the marine atmosphere (Endresen, 2003; Lauer et al., 2007; Lindstad et al., 2015; Marelle et al., 2016; Unger et al., 2010). In addition, a large fraction of ship PM is emitted near shore (Eyring et al., 2010), which has a strong potential to negatively impact human health (Corbett et al., 2007; Oeder et al., 2015) as well as visibility.

Ship engine PM contains significant amounts of organic PM (OM) as well as black carbon (BC; Buffaloe et al., 2014; Lack et al., 2009; Mueller et al., 2015; Price et al., 2016). When heavy fuel oil (HFO) is used, sulfates

also contribute significantly to PM mass (Lack et al., 2009; Mueller et al., 2015; Popovicheva et al., 2009). Typically, BC contributes a relatively small fraction to the mass of HFO PM. The overall single-scattering albedo (SSA) of HFO PM aerosols is therefore relatively high, such that ship-engine PM may result in an overall cooling over the (low-albedo) ocean surface (Lauer et al., 2007; Unger et al., 2010), but a localized warming over high-albedo surfaces or on snow and ice (Lack & Corbett, 2012). The accurate quantification of these radiative effects requires an accurate measurement of the light absorption properties of both BC and OM.

Light-absorbing OM has previously been inferred to contribute significantly to total HFO PM absorption at shorter visible wavelengths  $\lambda$ , based on the observation of  $2-\lambda$  absorption Ångström exponents (AAEs(370,880 nm), equation (1), much greater than unity (Mueller et al., 2015). Accounting for this light-absorbing OM in radiative models of the Earth's atmosphere requires knowledge of intensive optical properties, such as imaginary refractive index ( $k_{OM}$ ) and mass absorption cross section ( $MAC_{OM}$ ), which have not previously been reported.

A major goal of the present work was to quantify  $k_{OM}$  and  $MAC_{OM}$  for use in climate models. This quantification was achieved by applying the popular (Bahadur et al., 2012; Cazorla et al., 2013; Favez et al., 2009; Fialho et al., 2005; Grenfell et al., 2011; Lack & Langridge, 2013; Pokhrel et al., 2017; Sandradewi et al., 2008; Yuan et al., 2016; Zotter et al., 2017) two-component "BC + brC" model: (i) light absorption in the near infrared (e.g.,  $\lambda > 780$  nm) is attributed to BC only, (ii) BC absorption is assumed to depend inversely on  $\lambda$  ( $AAE_{BC} = 1$ ), and (iii) when measured visible light absorption exceeds predicted absorption by BC, the excess is attributed to light-absorbing OM (so-called brown carbon or brC). In this context, we define BC as refractory, light-absorbing carbon with an AAE of unity between  $370 \text{ nm} < \lambda < 950 \text{ nm}$  (Petzold et al., 2013). We consider BC as the sole light-absorbing species at  $\lambda \geq 780 \text{ nm}$  and, when the aerosol AAE exceeds unity, attribute the excess absorption to brC. While brC is therefore defined purely from the optical properties of the aerosol, we also calculate intensive brC properties by normalizing brC absorption to total organic PM mass.

For HFO PM, the two-component BC + brC absorption approach may not fully describe the aerosol. First, HFO exhaust may contain asphaltenes, large polyaromatic molecules that may contribute to PM light absorption in the near infrared, besides BC (Mullins, 2010). Second, light-absorbing char particles may also be present in HFO PM (Chen et al., 2005; Lyyränen et al., 1999; Popovicheva et al., 2009). These char particles are formed when fuel droplets graphitize rather than vaporize at the high flame temperatures (Linak et al., 2000) and are therefore a subcategory of BC, with typical physical diameters of  $\sim 1 \mu\text{m}$ . Their large physical diameter places char particles outside of the Rayleigh regime, potentially invalidating the  $AAE_{BC} = 1$  assumption of the BC + brC approach. Unfortunately, our present measurements do not provide sufficient information to address these char particles explicitly. To the extent that  $AAE_{char} \neq 1$ , our approach may overestimate or underestimate the absorption properties of brC. However, even if this was the case, our two-species (BC + brC) approach would still provide the optical parameters required for climate models to correctly represent the wavelength-dependent light absorption of HFO PM which we have observed; the inaccuracy would be in the relative attribution of absorption to the different light-absorbing species. Moreover, as demonstrated by Saleh et al. (2016), climate models which employ Mie theory in radiative transfer calculations produce more accurate estimates of radiative forcing when Mie-theory-retrieved parameters are used, compared to more-complex retrievals.

In the following, we determine the optical properties of brC from a ship engine operating on three different fuels: HFO, marine gas oil (MGO), and EN 590 diesel fuel (DF). The upcoming sections discuss (1) speciated PM emission factors and the PM mixing state, (2) the PM SSA and  $MAC_{BC}$  at 780 nm obtained by the extinction-minus-scattering technique combined with refractory BC (rBC) mass concentrations measured by a single-particle soot photometer (SP2), and (3) brC absorption using the BC + brC conceptual model in terms of  $MAC_{OM}$  and  $k_{OM}$  by using OM concentrations measured by an aerosol mass spectrometer (AMS). Note that the analysis in part (3) does not incorporate the SP2 measurements.

## 2. Methods

### 2.1. Experimental

The engine used in this study was a single-cylinder research engine installed at the Institute of Piston Machines and Internal Combustion Engines at the University of Rostock in Germany. The size of the combustion chamber and layout of the engine is typical of engines used on smaller ships as a main power supply, on large ships for ancillary power, or as a backup power supply on land, for example, in hospitals. The engine is

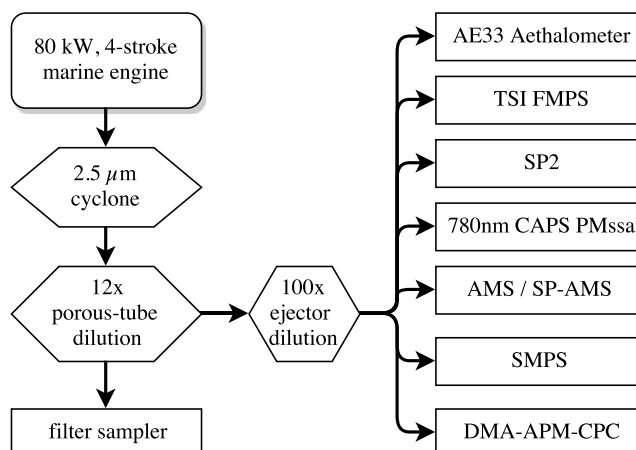


**Figure 1.** Experimental setup. Filter samples were measured after a factor  $\sim 12$  dilution; other measurements after a further factor 100 dilution. FMPS = Fast Mobility Particle Sizer; SP2 = single particle soot photometer; CAPS PMssa = Cavity Attenuation Phase Shift PM SSA monitor; AMS = Aerosol Mass Spectrometer; SMPS = Scanning Mobility Particle Sizer; APM = Aerosol Particle Mass analyzer.

of a four-stroke, single-cylinder design, with a 150-mm bore and 180-mm stroke and operates at a nominal 1,500 rpm with a maximum power of 80 kW. Previous publications have provided further details on the engine (Oeder et al., 2015; Streibel et al., 2017) and reported detailed characterizations of its emissions (Mueller et al., 2015); however, we emphasize that the engine was reconfigured between these two studies. During this study, certain engine operating parameters were varied to investigate their influence on the emissions; none of these parameters were identified as having influenced the properties discussed herein. The measurements took place between 10 November and 9 December 2014.

The sampling system was similar to that used by Streibel et al. (2017) and is shown in Figure 1. Emissions (sampled 1.5 m from the engine at  $> 500^\circ\text{C}$ ) were first passed through  $300^\circ\text{C}$  heated lines to a precyclone with a nominal cutoff aerodynamic diameter of  $2.5\ \mu\text{m}$  and then diluted by a factor of roughly 12 in a two-stage dilutor. The two-stage dilutor combined a porous-tube stage, where compressed air flowed through pores in a cylinder to provide a sheath flow and minimize wall losses, with an ejector dilutor, at a flow rate of 150 L/min. The exact dilution ratio was measured by real-time  $\text{CO}_2$  monitors. After this dilution stage, filter samples for thermal/optical reflectance analysis (resulting in NIOSH 5040 EC/OC data) and elemental analysis (discussed elsewhere; Corbin et al., 2018) were taken. Subsequently, two tenfold ejector dilutors (Dekati Ltd., Finland) were employed to reduce PM concentrations to atmospheric levels and ambient temperatures. The steel sampling line (10 mm i.d.) to the aethalometer was approximately 5 m long with a total flow of 4.5 L/min, while the other online instruments sampled at a total of 13 L/min through first  $\sim 7\text{-m}$  section of tubing and then at 3 L/min through a second 3-m section of tubing. This flow was then divided between similar lengths of line for the instruments.

The majority of the instruments sampled at high time resolution (1 min or faster), with the exception of the particle-filter samples. For the data presented below, the 30-min filter samples were generally used to define periods of interest (after manual inspection) and data were averaged over these periods.

Particle size distributions were obtained by a Scanning Mobility Particle Sizer (SMPS;  $^{85}\text{Kr}$  bipolar charger; Paul-Scherrer-Institute constructed differential mobility analyzer equivalent to the model 3081 of TSI Inc., United States; TSI CPC 3022A) and Fast Mobility Particle Sizer (FMPS, model 3091, TSI Inc.). The SMPS measurements are considered more reliable as data-inversion issues (influencing both sizing and counting) have been reported for the FMPS (Zimmerman et al., 2015). We therefore used the SMPS data to obtain geometric standard deviations (GSDs) of the size distribution for the Mie model. However, due to limited coverage of these SMPS data, the FMPS data were used to obtain geometric mean particle diameters (GMDs). These were retrieved from the FMPS data by fitting a bimodal lognormal function to the data using custom code written in Igor Pro (version 6.32, WaveMetrics, OR, United States). The FMPS data were first corrected using the routine

published by Zimmerman et al. (2015), which uses a separate CPC 3022A as a reference for the overall number concentration. The GMD obtained from the corrected FMPS data is considered more reliable than the FMPS GSD (Zimmerman et al., 2015).

For some samples, aerosol particle mass was measured for mobility-size-selected particles using a home-built DMA and a CPC (Model 3022A, TSI Inc. United States) sampling behind an Aerosol Particle Mass analyzer (APM Model 3601, Kanomax Japan). The DMA-APM-CPC data were analyzed as described in Zieger et al. (2017) to yield particle effective density measurements for the ultrafine mode, which was dominated by organics and sulfate. Considering that the organic-sulfate ultrafine particles were liquid and therefore spherical, these effective densities correspond directly to particle densities. Effective density measurements of rBC were attempted but were not feasible as the rBC number concentrations were much lower.

## 2.2. Single-Particle Soot Photometer

A Single-Particle Soot Photometer (SP2; Droplet Measurement Technologies, CO, United States) was employed to measure black carbon concentrations by laser-induced incandescence (Schwarz et al., 2006; Stephens et al., 2003). Data were analyzed using the PSI SP2 Toolkit, version 4.112. The SP2 brings BC-containing particles to incandescence during their passage through a continuous-wave, intracavity, 1,064-nm laser. The instrument detects rBC cores with mass (or volume-equivalent size,  $d_{\text{rBC}}$ , considering a void-free material density of  $1,800 \text{ kg m}^{-3}$ ) from  $\sim 0.7$  ( $\sim 80 \text{ nm}$ ) to  $\sim 200 \text{ fg}$  ( $\sim 600 \text{ nm}$ ). For particles in this size range, the total rBC mass reported by SP2 has been validated as accurate by multiple independent studies (Kondo et al., 2011; Laborde, Schnaiter, et al., 2012; Slowik et al. 2007). The total mass concentration reported below is corrected for the mass fraction outside of this range (section 3.1.1). We use the term “rBC” as recommended by Petzold et al. (2013) whenever reporting SP2 data in a quantitative manner, for example,  $C_{\text{rBC}}$  for BC mass concentrations and  $d_{\text{rBC}}$  for mass-equivalent diameters. We use the term rBC core to clarify that any nonrefractory, internally mixed material is not measured by incandescence as it vaporizes well below the  $\sim 4000 \text{ K}$  sublimation point of BC.

The SP2 also collects light-scattering signals, acting as an optical sizer for BC-free particles ( $d_{\text{minimum}} \approx 160 \text{ nm}$ ). For BC-containing particles, the scattering signal requires careful data processing because laser heating causes coatings to evaporate during measurement. This evaporation is observable in the time-resolved scattering signals. For uncoated or moderately coated particles, peak scattering signals occur when particles are relatively closer to the center of the Gaussian profile of the SP2 laser (since incident light intensity is highest closer to the center) and simultaneously with particle incandescence. For thickly coated particles, this peak is observed substantially earlier and prior to particle incandescence, corresponding to the substantial reduction in particle volume when coating material evaporates. This binary mixing-state classification is commonly referred to as “delay-time analysis” (Moteki & Kondo, 2007). On this basis, particles can be classified as either “thickly coated” (significant difference between peak scattering and incandescence signals) or “moderately or uncoated” (no significant difference). The lower detection limit for this classification is higher than that for rBC quantification, since the SP2 scattering measurement is less sensitive than the incandescence measurement. The upper limit for this classification is imposed by saturation of the scattering signal detector, which occurs for large overall particle sizes. We present data only for particles within these limits. Note that a particle consisting of an rBC particle coagulated with other material may appear to be thickly coated in the SP2, resulting in an overestimated fraction of thickly coated particles. Note also that a precise distinction between “moderate or no coating” and “thick coating,” for example in terms of BC volume fraction, cannot be given without knowledge of the thermochemical properties of the coating (Sedlacek et al., 2015). Based on our previous comparisons of coating thickness to delay-time data for atmospheric BC particles (unpublished work), we estimate that moderate or no coating describe particles containing 70–100% rBC volume.

A more complex data analysis approach allows the coating thickness of BC-containing particles to be retrieved quantitatively, as follows. By retrieving the scattering signal at 3% of the maximum laser intensity, at which point no coating material has yet evaporated, the scattering cross section of the total, possibly coated, particle can be determined (Gao et al., 2007; Taylor et al., 2015). Conversely, by retrieving the scattering signal after coatings have evaporated but before the onset of incandescence, the scattering cross section of uncoated rBC can be determined (Laborde, Mertes, et al., 2012). The latter value can be used to calculate the rBC-mass-equivalent volume of the rBC core, given a complex refractive index of the core  $m_{\text{core}} = (n, k)$ . The precise value of  $m_{\text{core}}$  is not well constrained and may vary between BC materials, but the empirical relationship  $k \approx (n - 1)$  has been shown by Bond and Bergstrom (2006), as discussed further by Moteki et al. (2010).

Employing this constraint, we determined  $m_{\text{core}}$  as  $1.9 + 0.8i$  by fitting the rBC-core volume determined by scattering to that determined by incandescence. Our approach of adjusting  $m_{\text{core}}$  only serves as an internal calibration of the coating-thickness retrieval and must not be misinterpreted as a measurement of the BC refractive index, which would require additional independent measurements. Our value of  $m_{\text{core}}$  is smaller than that typically used in SP2 analysis ( $2.26 + 1.26i$ ) but is consistent with that used by Laborde, Schnaiter, et al. (2012) for propane-flame soot. Using the typical  $m_{\text{core}}$  value of  $2.26 + 1.26i$  corresponds to smaller rather than larger coating thicknesses in the analysis presented below. We note that it is typical to observe some negative coating thicknesses in this analysis due to random noise on the single-particle level. Investigations in our laboratory have found that this noise is due mainly to the variability of particle velocity through the laser beam and uncertainty in determining the scattering signal at 3% of the maximum laser intensity. The retrieval of the scattering signal at 3% of the maximum laser intensity means that the lower detection limit for coating-thickness analysis is substantially higher than for delay-time analysis.

The SP2 was operated and calibrated as described in (Laborde, Schnaiter, et al., 2012). Briefly, mass-selected rBC particles representative of atmospheric or diesel rBC (Alfa Aeser Inc., FS, Lot #FS12S011) were used to calibrate the peak incandescence signal and polystyrene latex sphere standards of diameter 269 nm were used to calibrate the partial scattering cross-section measurements.

### 2.3. Aerosol Mass Spectrometer

Particles are introduced into the High-Resolution Aerosol Mass Spectrometer (AMS) by an aerodynamic lens (Liu et al., 2007), which has its maximum transmission efficiency between about 100 to 600 nm in free-molecular aerodynamic diameter ( $d_{\text{fm,a}}$ ). Note that this aerodynamic diameter is weighted by particle density (Kulkarni et al., 2011), so that  $d_{\text{fm,a}} = 100$  nm corresponds to a volume-equivalent diameter of 69 nm for the HFO PM density reported below. Nonrefractory material in these particles is then vaporized by an 873 K porous-tungsten cone before electron ionization. The resulting ions are analyzed in a high-resolution time-of-flight mass spectrometer (DeCarlo et al., 2006). Note that we have used the term “sulfate” below rather than “sulfuric acid” (the likely form of sulfate, as discussed below) because sulfate and nitrate are the chemical components measured by AMS after electron ionization. For a more detailed discussion of the AMS results of this study, see Corbin et al. (2018).

### 2.4. Optical Measurements

The aerosol absorption coefficient was measured by the extinction-minus-scattering technique, using a Cavity Attenuation Phase Shift PM SSA monitor (CAPS PMssa, Onasch et al., 2015) operating at 780 nm. This instrument provides a calibration-free measure of extinction (manufacturer-estimated accuracy: 5%). The extinction measurement occurs in an optical cell which incorporates an integrating-sphere nephelometer. This nephelometer was calibrated using the extinction measurement, as described in Onasch et al. (2015), using 269-nm-diameter polystyrene latex spheres and size-selected  $\text{NH}_4\text{NO}_3$ . We also performed a calibration at the Paul Scherrer Institute using pure  $\text{N}_2$  and  $\text{CO}_2$ . Overall, eight calibrations over 13 months using all of these approaches showed a relative standard deviation of only 10%, indicating very stable instrument performance. Data were manually inspected to ensure that baseline values of extinction and scattering (obtained periodically on filtered samples) were stable. Note that during engine measurements, the CAPS PMssa was occasionally diluted by a factor of 5.1 owing to flow limitations in some experiments (not presented here), which was tested and found to have no effect on the resulting data.

Some data were also acquired using CAPS PMssa instruments operating at 450 and 630 nm. These data are not presented here due to issues with data quality, possibly due to the difficulty of obtaining a valid baseline measurement when variable amounts of absorbing gases with strong surface interactions, such as  $\text{NO}_2$ , are present.

An aethalometer (model AE33, Aerosol d.o.o., Slovenia) was also deployed during these experiments. The AE33 measures the light attenuation through a PM deposit on a filter at seven wavelengths  $\lambda$ . The AE33 converts filter-deposit attenuation coefficients to aerosol light absorption coefficients by applying a conversion factor (known as the “C value”) as detailed in Drinovec et al. (2015) and discussed further in section S3, where the calibration factor is evaluated for our samples at 780 nm. To avoid issues due to pressure changes in the sampling lines due to changes in engine conditions, our AE33 data were reanalyzed with a constant compensation parameter (defined in Drinovec et al., 2015).



Three filter samples were also measured with the Multiwavelength Absorbance Analyzer (MWAA; Massabò et al., 2015) with the goal of evaluating the performance of the CAPS PM<sub>ss</sub>. In particular, the wavelength dependence of the aethalometer calibration could be confirmed as negligible using the MWAA data. This is evident in Figure 6, as discussed further in the supporting information.

## 2.5. Optical Calculations

Using the AE33 data, the AAE was calculated as the two-wavelength AAE:

$$AAE(\lambda_1, \lambda_2) = -\frac{\ln(b_{ATN,\lambda_1}/b_{ATN,\lambda_2})}{\ln(\lambda_1/\lambda_2)} \quad (1)$$

where the subscripts 1 and 2 indicate two different measurement wavelengths,  $\lambda$  is a measurement wavelength, and  $b_{ATN,\lambda}$  is an AE33-measured attenuation coefficient.

Using the CAPS PM<sub>ss</sub> data,  $b_{abn,\lambda}$  was calculated at  $\lambda = 780$  nm by subtracting the measured scattering from the measured extinction coefficient. By combining the CAPS PM<sub>ss</sub>  $b_{abn,780}$  with the measured AAEs, we also calculated  $b_{abn,\lambda}$  at  $\lambda = (370, 470, 520, 590, 660, 880, 950)$  nm. This calculation is numerically equivalent to calibrating the aethalometer using the CAPS PM<sub>ss</sub> (full details are given in the supporting information). For some samples, CAPS PM<sub>ss</sub> data were not available for this calibration, and the median  $C$  value from the other calibrations was applied.

The MAC of a species  $X$  at a wavelength  $\lambda$ ,  $MAC_{X,\lambda}$ , was calculated as

$$MAC_{X,\lambda} = b_{abn,X,\lambda}/C_X, \quad (2)$$

where  $b_{abn,X,\lambda}$  is the aerosol absorption coefficient corresponding to absorption by species  $X$ . In general, brC is considered to absorb negligibly at longer wavelengths (Laskin et al., 2015), so that we attribute all absorption at  $\lambda \geq 780$  nm to BC ( $b_{abn,BC,\lambda} \approx b_{abn,\lambda}$ ) and the equation becomes

$$MAC_{rBC,780} = b_{abn,BC,780}/C_{rBC} \approx b_{abn,780}/C_{rBC}, \quad (3)$$

for BC, with  $C_{rBC}$  measured by the SP2, corrected for the mass fraction outside of the SP2 sensitivity range (section 3.1.1).

Light absorption was attributed to brC when the measured absorption exceeded that predicted by extrapolating measurements at longer wavelengths ( $\lambda \geq 780$  nm) to shorter ones ( $\lambda \leq 660$  nm) using an  $AAE = 1$ . That is, brC absorption was defined by

$$b_{abn,brC,\lambda} = b_{abn,\lambda} - b_{abn,BC,880} \left( \frac{\lambda}{880 \text{ nm}} \right)^{-AAE_{BC}}, \quad (4)$$

where  $\lambda$  and 880 nm represent two measurement wavelengths in nanometer nanometers (missing s) and the subtracted quantity is the AAE-based estimate of BC absorption at  $\lambda$ , using  $AAE_{BC} = 1$  except during sensitivity tests (see below). Equation (4) results in a positive value of  $b_{abn,brC,\lambda}$  when  $AAE_{PM} > 1$  and zero  $b_{abn,brC,\lambda}$  when  $AAE_{PM} = 1$ . In no case was  $AAE_{PM} < 1$ . While both  $b_{abn,\lambda}$  and the AAE may be affected by substantial internal mixing (Lack & Cappa, 2010), we expect this effect to be negligible in our data because substantial internal mixing of brC and BC was ruled out by our measurements (section 3.1.2). Equation (4) was employed to calculate  $b_{abn,brC,\lambda}$  at  $\lambda = \{370, 470, 520, 590, 660\}$  nm, corresponding to each measured wavelength shorter than the reference (CAPS PM<sub>ss</sub>)  $\lambda = 780$  nm.

As shown in equation (4), we generally used  $\lambda_2 = 880$  nm as the reference wavelength. A sensitivity test using  $\lambda_2 = 950$  nm changed the calculated brC absorption by HFO by only  $<2\%$  on average. (HFO was the only fuel with  $AAE_{PM}$  substantially higher than unity.) Uncertainties in the use of equation (4) are discussed in section 2.7.

The MAC of brC was calculated using equation (2) with  $b_{abn,brC,\lambda}$  and  $C_{OM}$  substituted for  $b_{abn,X,\lambda}$  and  $C_X$ , respectively:

$$MAC_{OM,\lambda} = b_{abn,brC,\lambda}/C_{OM}, \quad (5)$$

where  $C_{OM}$  is the OM mass concentration measured by the AMS.

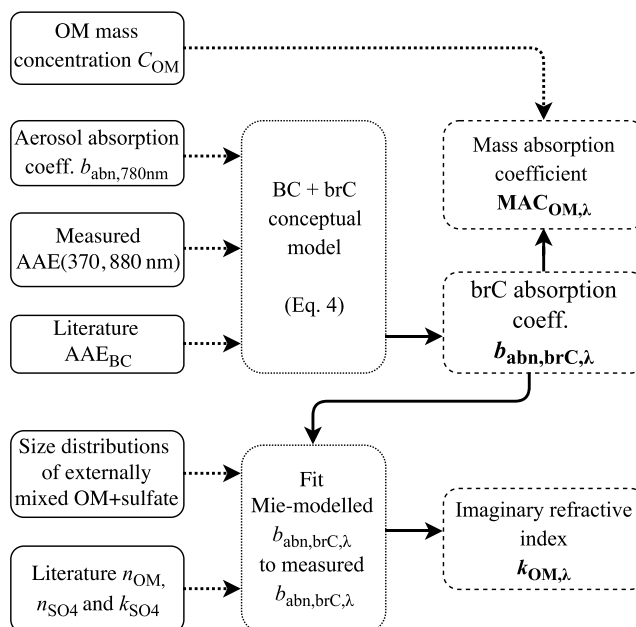


**Figure 2.** Schematic of the BC + brC analysis and Mie model fit performed herein. Symbols and abbreviations are defined in Table 1.

### 2.6. Mie Model

A Mie model was constructed and fitted to the brC absorption and OM mass concentration measurements to obtain imaginary refractive indices of OM,  $k_{OM}$ . The model structure, inputs, and outputs are depicted in Figure 2 and described in the following.

As described below, our measurements indicated that these ship-engine emissions can be appropriately modeled as an external mixture of two modes, a larger rBC mode and a smaller nucleation mode (internally mixed OM and sulfate). In estimating  $b_{abn,brC,\lambda}$  from equation (4), we have already subtracted light absorption by BC from the total and must only model the brC absorption when fitting the Mie model.

The model therefore consisted of a single lognormal distribution of internally mixed sulfates and OM; the reported  $k_{OM}$  values were obtained by minimizing the difference between the measured absorption and the Mie-predicted absorption of this distribution (each reported  $k_{OM}$  was fitted independently of the others). The Mie calculations required several additional pieces of information, which were constrained as follows. The GMD was obtained from bimodal lognormal fits to the FMPS measurements, and a GSD of 1.65 was obtained from the SMPS data as described in section 2.1. The respective fractions of OM and sulfate in the particles were obtained from the AMS data. The particle material density was obtained from the DMA-APM measurements described above. For HFO and MGO PM, the respectively measured material densities were  $1,460 \pm 50$  and  $900 \pm 40$  kg/m<sup>3</sup>. The higher density for HFO PM is due to the presence of sulfate. The density measurements of MGO PM were also used to estimate the density of DF PM, which was not measured. The measured densities are in good agreement with the density estimated from the mass spectra of these samples (Kuwata et al., 2012), as described in the supporting information.

The real refractive index of OM,  $n_{OM}$ , was taken as  $n = 1.5$  (Lu et al., 2015); the fitted results did not change when varying this value as  $n_{OM} \pm 0.1$ . The corresponding  $n_{SO_4^{2-}}$  was taken as 1.35 (sulfuric acid). The overall refractive index of the particles was obtained by combining  $n_{OM}$  and  $n_{SO_4^{2-}}$  according to their AMS-measured volume ratios, following the volume-weighted linear mixing rule validated by Abo Riziq et al. (2007). Sensitivity tests indicated that the most sensitive input parameter in this model was the GMD: a large change in GMD of 20 nm corresponded to a change of only  $\pm 0.001$  in  $k_{OM}$  ( $k_{OM}$  was greater than 0.01 for all HFO samples, as shown in Figure 8 below). Varying other parameters by large amounts (relative to their anticipated uncertainties) generally led to <10% change in  $k_{OM}$ . We note that the PM density used here was well constrained by the APM measurements.

**Table 1**  
Common Abbreviations and Symbols Used in the Text

Abbreviation	Definition
AAE	Absorption Ångström exponent
AAE( $\lambda_1, \lambda_2$ )	AAE calculated from two specified $\lambda$
AE33	Model AE33 Aethalometer
BC	Black carbon
rBC	refractory BC, measured by SP2
brC	Brown carbon, operationally defined by light absorption in excess of that predicted for BC
CAPS PM <sub>ssa</sub>	Cavity Attenuation Phase Shift PM SSA monitor
AMS	Aerosol Mass Spectrometer
APM	Aerosol Particle Mass analyzer
DF	Diesel fuel (a distillate fuel)
MAC	Mass absorption cross section of PM
MGO	Marine Gas Oil (a distillate fuel)
MWAA	Multiwavelength Absorption Analysis
HFO	Heavy fuel oil (residual fuel)
OM	The nonrefractory organic component of PM, operationally defined by vaporization at 600 °C
PM	Particulate matter
SSA	Single-scattering albedo
SP2	Single-Particle Soot Photometer
$b_{\text{abn}}$	Aerosol absorption coefficient
$C_x$	Mass concentration of $x$
$n$	Real part of the refractive index
$k$	Imaginary part of the refractive index
$\lambda$	Wavelength
$d_{\text{rBC}}$	Volume-equivalent diameter of rBC core
$d_{\text{mob}}$	Mobility diameter

Note. Rarely used abbreviations have been omitted for brevity.

Overall uncertainties in  $k_{\text{OM}}$  were calculated by propagating the numerical uncertainties given below in a Monte Carlo calculation.

### 2.7. Statistical Uncertainties

Unless specified otherwise in this section, uncertainties are statistical imprecisions and are reported as the standard error of the mean ( $\sigma_{\bar{x}} = SD/\sqrt{N}$ ),  $SD$ , standard deviation) with the averaging periods defined by the 30-min filter periods mentioned above. For derived quantities, uncertainties were propagated from these  $\sigma_{\bar{x}}$ .

In the special cases where uncertainties other than statistical noise were known to be significant, those uncertainties were added in quadrature (i.e., possible covariance between these different uncertainties was not addressed):

1. For the CAPS PM<sub>ssa</sub>, uncertainties in  $b_{\text{abn}}$  were propagated from an estimated 5% accuracy in  $b_{\text{ext}}$  (as estimated by Onasch et al., 2015), 10% accuracy in scattering calibration (based on the SD of multiple calibrations),  $\pm 1 \text{ Mm}^{-1}$  baselining accuracy and 5% accuracy in dilution correction. The fraction of scattered light not collected by the CAPS PM<sub>ssa</sub> integrating sphere (the truncation error) must be corrected for if the phase function of measured particles is substantially different to that of the calibration particles. This is not the case if both measured and calibration particles are small relative to the 780-nm wavelength of the CAPS Onasch et al. (2015), which was generally true. Any potential complications introduced by the larger BC



- mode in HFO PM are unlikely, considering the fact that the HFO data were not outliers in the optical analyses described below. We note that the calculated absorption is not highly sensitive to truncation errors at low SSA values ( $\sim 0.7$ ).
2. For the SP2, the relatively low number of rBC particles measured in each sampling period yielded substantial statistical imprecision, which is the major source of reported uncertainty. Calibration-related uncertainties were not propagated into the reported uncertainties; the precision of our calibration data was much less than the just-mentioned statistical imprecision. An unknown source of uncertainty is calibration bias related to differences between calibrant and sample. To the extent that marine engine rBC is similar to road-vehicle rBC, the latter bias is estimated as  $<14\%$  (Laborde, Mertes et al., 2012).
  3. For the AMS, a measurement precision of  $0.3 \mu\text{g}/\text{m}^3$  was estimated from measurements of filtered air and combined with the statistical imprecision of the mean. Measured concentrations may have been biased low by  $\sim 10\%$  to  $35\%$ , for smaller particles, due to the small measured particle sizes (e.g.,  $\sim 60\text{-nm}$  mode diameter of volume distributions). This size-dependent bias was discussed by Liu et al. (2007). Other known biases (Jimenez et al., 2016) include variability in the electron ionization efficiency of different organic molecules and the partial loss of particles to bounce off of the heated vaporizer. The former effect was treated as negligible and the latter estimated as negligible since these particles contained a substantial amount of lubrication oil (Eichler et al., 2017), which as a liquid is unlikely to bounce (Jimenez et al., 2016).
  4. An estimated inaccuracy of  $\sigma_{\text{AAE(BC)}} = 0.1$  was propagated into the calculated uncertainties of  $b_{\text{abn,brC},\lambda}$ .
  5. In calculating  $k_{\text{OM}}$ , estimated imprecisions of  $5 \text{ nm}$  in GMD,  $0.1$  in GSD, and  $4\%$  in density (from the SD of multiple measurements) were considered as Gaussian and propagated by Monte Carlo calculation.

### 3. Results and Discussion

#### 3.1. Engine Emissions

The emission factors relative to engine power (in units of  $\text{mg}/\text{kWh}$ ) for OM, sulfates, rBC, and nitrates from this engine were similar to those reported by Mueller et al. (2015) for this engine. For all three fuels, OM emissions dominated the total PM mass with little sensitivity to engine load. For HFO, OM contributed  $58\%$  of the  $\text{PM}_{2.5}$  mass at  $50\%$  load (because sulfate contributed  $25\%$ ) and  $>82\%$  of the  $\text{PM}_{2.5}$  mass below  $50\%$  load. Notably, when normalized to  $\text{CO}_2$  rather than engine power, the variability in emission factors for rBC was substantially reduced. Section S1 provides more detail on these emission factors.

##### 3.1.1. Total and BC Size Distributions

Particle number and volume size distributions, as measured by SMPS as a function of mobility diameter  $d_{\text{mob}}$ , are shown in Figure 3. Also shown in these figures are the number and volume distributions of rBC cores, as measured by SP2 as a function of  $d_{\text{rBC}}$ . These size distributions are representative averages of selected measurement periods, where both SMPS and SP2 data were available.

The size distributions of the DF and marine gas oil (MGO) PM, shown in Figure 3, were comparable to that of typical diesel engines (Burtcher, 2005), in that two separate modes are identifiable, a volatile ultrafine mode (at about  $60 \text{ nm}$   $d_{\text{mob}}$  in the total-volume distribution) and a soot mode (lognormal at about  $120 \text{ nm}$   $d_{\text{rBC}}$  in the rBC volume distribution) were observed. AMS measurements of the fresh and thermodenuded aerosol indicated that the ultrafine mode for these distillate fuels consisted mainly of organics and, for MGO, sulfates. The rBC volume distribution indicated that a fraction of the MGO and DF particles was above or below the quantification range of the SP2, corresponding to an unmeasured mass fraction of  $<3\%$  (above) and  $<23\%$  (below), respectively. The rBC mass concentrations reported from these SP2 data have been corrected for this missing fraction, as discussed further at the end of this subsection.

In considering Figure 3 relative to previous studies (Mueller et al., 2015; Oeder et al., 2015; Streibel et al., 2017), it is important to realize that the SP2-measured  $d_{\text{rBC}}$  is a volume-equivalent diameter, which is by definition smaller than  $d_{\text{mob}}$  for soot particles of both open and compact morphologies (Kulkarni et al., 2011). For the two size distributions in Figure 3 to overlap, a size-independent shape factor of  $\sim 2.2$  is required. This value is within the range of values ( $1.5$ – $3$ ) recommended by Sorensen (2011) for uncoated, fractal-like BC aggregates and corresponds to  $\sim 50$  primary particles in a typical BC aggregate, if the monomer diameter is  $30 \text{ nm}$  (this monomer diameter is from Oeder et al., 2015). Thus, our measured size distributions are consistent with the evidence presented in section 3.1.2 to demonstrate that rBC was externally mixed.

The size distribution of the residual fuel, HFO, also showed an ultrafine mode consisting of sulfates and organics with a mode mobility diameter of about  $90 \text{ nm}$ . This mode dominated the overall particle number and had a mean ( $\pm$ SD) effective density of  $1,460 \pm 50 \text{ kg}/\text{m}^3$ . The effective density was considerably lower for MGO,

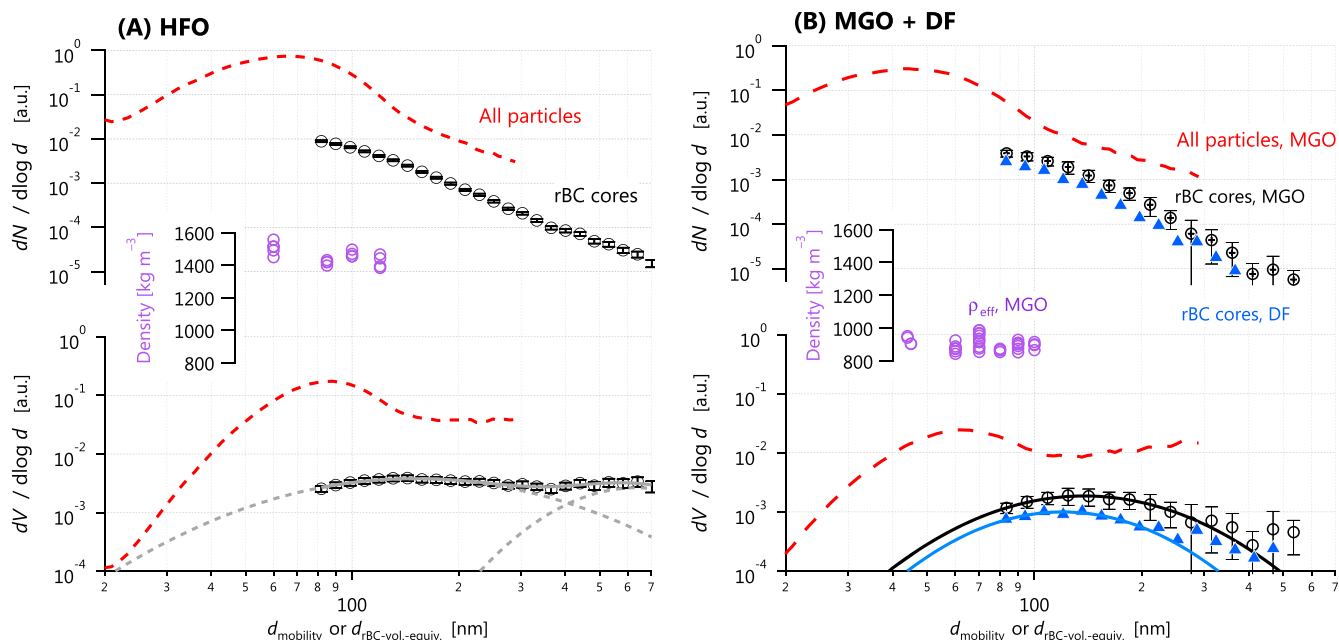


**Figure 3.** Size distributions of PM from the marine engine operated on (a) HFO and (b) MGO and diesel. Inset are the DMA-APM effective density data. The upper tails of the total (red; SMPS) distributions do not overlap the rBC distributions (black and blue) because of significant uncertainties in volume calculation for large, irregular particles, and because the latter is plotted against volume-equivalent rBC diameters, which are smaller than mobility diameters for coated or aspherical particles (see text). SMPS measurements for diesel are not available. SMPS = Scanning Mobility Particle Sizer; HFO = heavy fuel oil; rBC = refractory black carbon; MGO = marine gas oil; APM = Aerosol Particle Mass.

at  $890 \pm 30 \text{ kg/m}^3$  (data shown in Figure 3). The effective densities for DF PM were not measured. Since the particles consisted of organics and sulfate (see also section 3.1.2) they were liquid (Seinfeld & Pandis, 2012), and these effective densities correspond directly to the material density of this PM mode. We could not obtain effective density measurements of rBC-containing particles due to their relatively low number concentrations.

The rBC-core distribution showed a much broader volume distribution than is expected for vehicular (Burtscher, 2005; Laborde, Crippa et al., 2012), biomass burning (Laborde, Crippa, et al., 2012; Schwarz et al., 2008; Wang et al., 2016), or aircraft (Lobo et al., 2015) emissions. Two studies of Chinese air pollution have also reported large rBC modes of 690 (Huang et al., 2011) and 610 nm (Wu et al., 2017), which may be linked to HFO-combustion pollution. In HFO exhaust from a marine diesel engine, Kasper et al. (2007) also observed a large, nonvolatile (at  $400^\circ\text{C}$ ) mode but did not measure its chemical composition. Our measurements show that at least part of this mode likely consisted of rBC. It likely comprised the char particles defined in section 1. Future studies should further explore the properties of this large rBC mode.

The SP2 did not measure the tail of the hypothesized char mode (larger rBC mode). In the laboratory, Linak et al. (2000) found that char particles produced from HFO had a typical diameter of  $1 \mu\text{m}$ , which may correspond to the significant mass fraction of PM that has been identified in the coarse mode of marine engines (Fridell et al., 2008). Therefore, we initially hypothesized that the SP2 may not have measured all BC mass in the aerosol. However, we did not find supporting evidence for this hypothesis, as discussed in the following paragraphs.

A simple test of this hypothesis may be performed using the SP2 data directly. At the upper limit of single-particle mass, single particles are measured as saturated signals in the SP2. For the HFO size distribution presented in Figure 3 only 5 of 350,000 particles caused saturated signals. Therefore, the majority of the PM passing through our sampling system (which included a  $\text{PM}_{2.5}$  cyclone) and reaching the SP2 was measured. This conclusion is corroborated by the excellent correlation between CAPS  $\text{PM}_{2.5}$  and SP2 (Figures S1 and S2), for which data were available only for selected experiments.

Another test of this hypothesis was performed using Mie calculations of the AAE(880,950) for BC and for cenospheres. We chose this wavelength pair so that absorption by canonical brC would be negligible (Laskin et al., 2015). Cenospheres are core-shell BC particles with air cores and have been observed in HFO PM

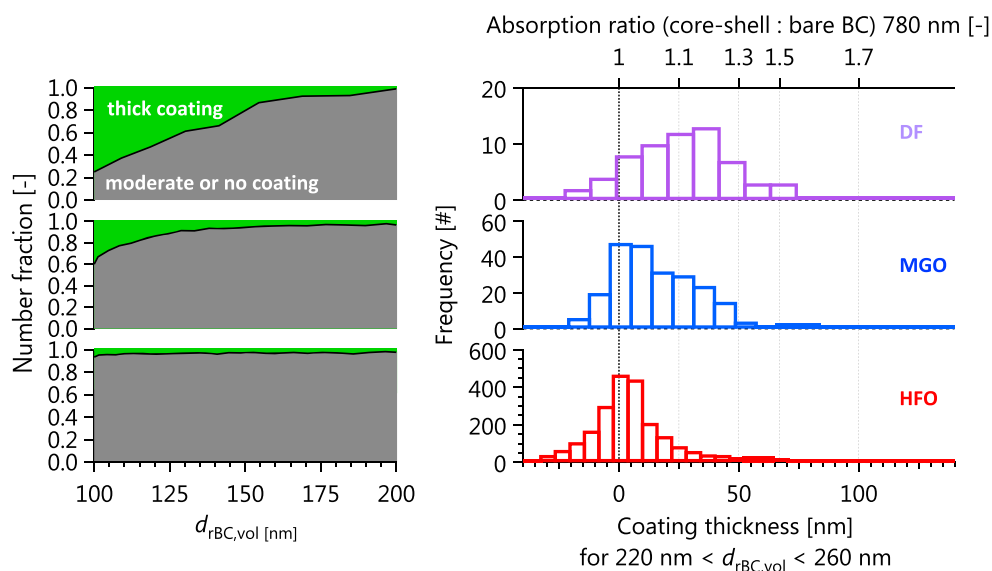


**Figure 4.** (a) Number fractions of particles with thick coatings versus moderate or no coatings, as determined by SP2 delay-time analysis, for BC-containing particles with  $d_{rBC}$  100 to 200 nm. (b) SP2 coating thicknesses of BC-containing particles with  $d_{rBC} = 240 \pm 20$  nm. Negative coating thicknesses are due to noise, as discussed in the text. Note that the histogram for HFO represents an order of magnitude more data than the other fuels, due to practical constraints. Note also that different  $d_{rBC}$  ranges size range are shown in (a) and (b) due to the fundamental difference of the two analyses (see text). The upper axis in (b) shows the predicted core-shell-Mie absorption enhancement for these coating thicknesses at the 780-nm wavelength of the CAPS PM<sub>ssa</sub>. CAPS PM<sub>ssa</sub> = Cavity Attenuation Phase Shift PM SSA monitor; BC = black carbon; rBC = refractory black carbon; HFO = heavy fuel oil. SP2 = single particle soot photometer.

(e.g., Chen et al., 2005). They may be modeled accurately with core-shell Mie theory (Huang et al., 2012), which we have done in Figure S3. The cenospheres were modeled with a ratio of inner to outer diameters of 0.8 (the abscissa of Figure S3 is the outer diameter).

The Mie calculations (Figure S3) show that in the Rayleigh regime (diameter  $d < 30$  nm) the predicted  $AAE_{BC} \approx 1$  does not depend on the model, as expected. Outside of the Rayleigh regime ( $d > 400$  nm), the model becomes important; in our calculations the  $AAE_{BC} \approx 0$ . The calculated  $AAE_{BC} \approx 0$  is much smaller than our observed  $AAE(880,950) \geq 1$  (also shown in the figure), suggesting that the majority of BC absorption and therefore BC mass did not reside in unmeasured char particles.

Overall, the HFO rBC size distribution could be described by a bimodal lognormal fit with geometric mean  $d_{rBC}$  and standard deviations (GMD and GSD) of 150 and 640 nm, and 1.0 and 0.56, for the two modes. These lognormal fits imply that 44% of the total mass was likely above (versus 2% below) the particle size range detectable by the SP2 and were used to correct the total reported rBC mass. The corresponding SP2-mass correction factor was  $1.46 \pm 0.15$ . This uncertainty represents interexperiment variability and was propagated into the overall uncertainty. For unimodal lognormal fits to the diesel and MGO data, the correction factors were  $1.247 \pm 0.05$  and  $1.228 \pm 0.05$ , respectively. These latter correction factors account for particles that were too small to be measured by the SP2.

### 3.1.2. External Mixing of rBC and OM/Sulfate

Figures 4a and 4b investigate the coating thickness on BC particles by analyzing the time-resolved SP2 scattering signals in two different ways. Figure 4a shows that the number fraction of particles with evidence of “thick coatings” (where the peak scattering signal occurs before particle incandescence, indicating the loss of a large volume of coating material due to heating) was negligible except for smaller DF particles. (Since no rBC absorption was observed for DF, this exception does not influence any of the conclusions made in this study.) The remainder, “moderate or no coating,” describes particles where peak scattering occurred simultaneously with incandescence. This delay-time analysis provides a relatively coarse picture of the mixing state of BC; more quantitative information is provided by the coating-thickness analysis.

Figure 4b shows the results of the SP2 coating-thickness analysis. For this analysis, only BC particles with spherical-equivalent diameter  $240 \pm 20$  nm were included, due to the need to optimize both counting

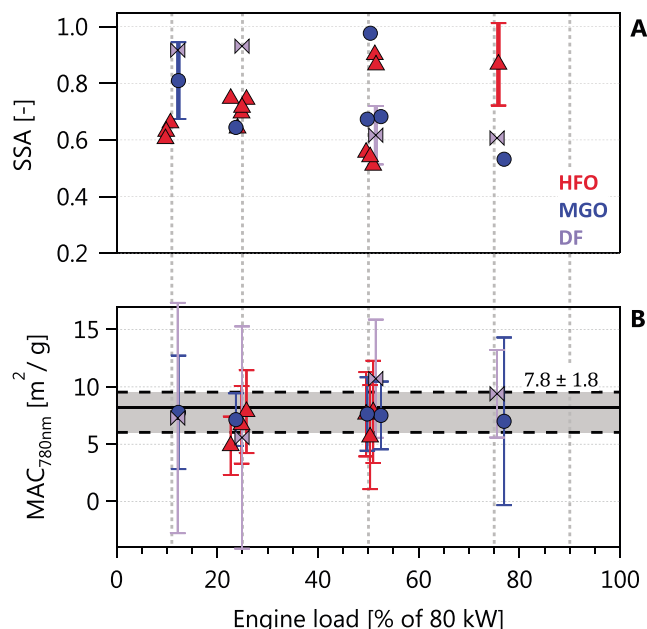


**Figure 5.** MAC and SSA for the three fuels as a function of engine load. No trend with engine power or fuel is apparent. Only three error bars are shown in (a) for clarity. The shaded area in (b) reflects a  $MAC_{rBC,780nm}$  of  $7.8 \pm 1.8 \text{ m}^2/\text{g}$  (fit  $\pm$  standard error). SSA = single-scattering albedo; HFO = heavy fuel oil; MGO = marine gas oil; DF = diesel fuel; MAC = mass absorption cross section; rBC = refractory black carbon.

statistics and signal-to-noise in the SP2 detectors. Consistent with the delay-time analysis, the coating-thickness results show that the mean coating thickness for HFO particles was negligible, whereas small amounts of coatings may have been present for MGO and DF. Negative coating thicknesses reflect particle-to-particle errors (biases) in the scattering measurements, which average to zero. Note that an order of magnitude more data were available for the HFO analysis than for the other fuels analysis. In all cases, the analysis indicates that the coatings were not thick enough to influence the optical properties of the BC (Liu et al., 2017).

Further analysis of independent size-resolved composition measurements for HFO (Corbin et al., 2018) support this picture. Ash (metal oxides and/or sulfates) is also expected in the HFO PM, as discussed in Corbin et al. (2018). However, with the measurements presented here, we can only infer that ash particles did not make up the majority of the total particle mass for either rBC or OM/sulfate particles.

The effective density measurements for the mobility size range 60–120 nm shown in Figure 3 also support our conclusion that the smaller mode in that figure consisted of externally mixed OM (and sulfate, in the case of HFO). The effective densities (calculated as  $6m_p/[\pi d_{mobility}^3]$ , where  $m_p$  is the APM-measured single-particle mass and  $d_{mobility}$  is the DMA-selected diameter, as further described in the supporting information) are shown by the inset circles in Figure 3. For MGO and DF, these densities should correspond to the material density of the OM in those fuels. Indeed, the measurements are in close agreement with the densities predicted from a published empirical relationship between the elemental composition and the density of OM (Kuwata et al., 2012). That parameterization showed a low bias of just 5% (standard deviation 2%) relative to the DMA-APM-CPC measurements.

### 3.1.3. Relationship of BC Light Absorption With $SSA_{780nm}$ and Engine Load

BC light absorption was characterized according to the aerosol light absorption coefficient measured at 780 nm,  $b_{abn,780nm}$ , which was measured by the CAPS PM<sub>ssa</sub> using the extinction-minus-scattering technique. The measured extinction and scattering coefficients also provided the aerosol  $SSA_{780nm}$  (Figure 5a). All three fuels showed a range of  $SSA_{780nm}$  (from 0.5 to 0.9). The lower SSAs correspond to conditions where the extinction-minus-scattering method results in a more accurate calculation of  $b_{abn,780nm}$ .

The ratio of CAPS  $b_{abn,780nm}$  to SP2  $C_{rBC}$  gives the  $MAC_{BC,780nm}$  (equation (3), as shown in Figure 5b). The observed  $MAC_{BC,780nm}$  did not vary substantially between engine loads and fuel types. The  $SSA_{780nm}$  did vary substantially but without a clear dependence on engine load, fuel type, or indeed any other parameter we evaluated,

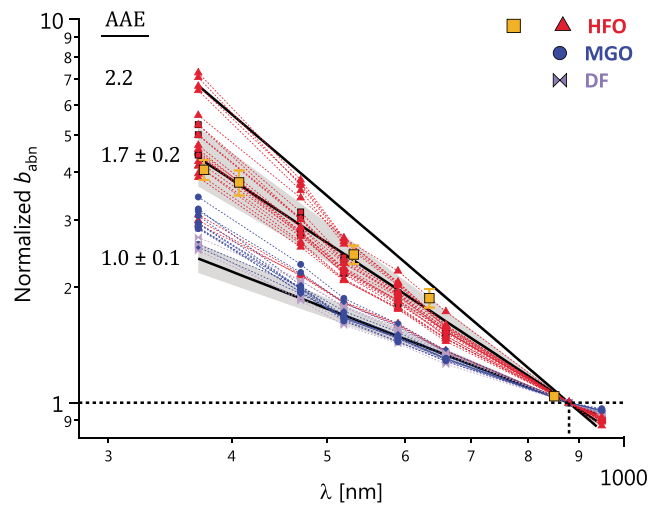


**Figure 6.** Measured absorption spectra for all engine test points, normalized to 880 nm. The black lines and shading indicate power laws (AAEs) and uncertainties of 2.2,  $1.7 \pm 0.2$ , and  $1.0 \pm 0.1$ , as labeled. All data are from the AE33 except the orange squares, which are MWAA measurements of filter samples (using a normalization factor of 0.96 to adjust from 850 to 880 nm based on an AAE = 1.7; simultaneous AE33 measurements are highlighted with red squares). MWAA = Multiwavelength Absorbance Analyzer; HFO = heavy fuel oil; MGO = marine gas oil; DF = diesel fuel; AAE = Ångström exponent.

including the GMD (geometric mean diameter of the FMPS) and the ratio BC:nonrefractory PM. These quantities were explored because it was expected that the  $MAC_{BC,780nm}$  and  $SSA_{780nm}$  would vary as a function of aerosol composition (e.g., the mass fraction of BC), size (since scattering depends strongly on particle size), or mixing state (since internal mixing of BC with other material may result in absorption enhancements). Note that although the accuracy of the CAPS-estimated  $b_{abn,780nm}$  is expected to decrease with increasing SSA, our data indicate that this accuracy was not a limiting factor: there was no statistically significant dependence of the  $MAC_{BC,780nm}$  on the SSA.

The lack of any such observed relationship indicates that the corresponding phenomena were not the main cause of variations in the  $SSA_{780nm}$ . Moreover, the fact that variations in  $SSA_{780nm}$  did not correspond to variations in  $MAC_{BC,780nm}$  is consistent with the aerosol containing a variable fraction of externally mixed BC. We therefore hypothesize that variable amounts of externally mixed ash particles were the main cause of the variability in the  $SSA_{780nm}$ . Such ash particles were identified by electron microscopy in these samples (Corbin et al., 2018), but more data would be needed to quantitatively evaluate this hypothesis.

The shading in Figure 5b shows the result of an uncertainty-weighted orthogonal-distance regression fit to a plot of  $b_{abn,780nm}$  versus  $C_{rBC}$  (the shading shows the fit  $\pm 95\%$  confidence interval; Figure S1). As there was no apparent difference in  $MAC_{BC,780nm}$  between different fuels, all data were fit simultaneously to yield  $MAC_{BC,780nm} = 7.8 \pm 1.8 \text{ m}^2/\text{g}$ . Assuming an  $AAE_{BC}$  of 1, this corresponds to a  $MAC_{rBC,550nm}$  of  $11.1 \pm 2.6$ , a factor 1.48 larger than the widely accepted  $MAC_{BC,550nm} = 7.5 \text{ m}^2/\text{g}$  recommended by Bond and Bergstrom (2006) for uncoated BC.

An increase in MAC due to so-called lensing effects may occur if rBC is internally mixed with substantial amounts of nonabsorbing material (Liu et al., 2017). However, our SP2 measurements indicate that much more internal mixing than observed would be necessary to explain a 48% lensing enhancement (Figure 4). The calculated absorption enhancement for a 240-nm rBC core is shown on the upper axis of Figure 4, using a Mie approximation. For HFO, a negligible enhancement is predicted. For MGO and DF, a maximum absorption enhancement of 10–20% is predicted. Further calculations verified that these enhancements change negligibly when the soot aggregates are represented as noninteracting monomer spheres, instead of volume-equivalent spheres (Liu et al., 2015). Considering the uncertainties associated with the coating-thickness and MAC data, we consider that the discrepancy between the calculated and apparent absorption enhancements is probably negligible for MGO and DF. For HFO, where our confidence is enhanced by a larger number of analyzed particles, we find that lensing does not explain why the  $MAC_{rBC,780nm}$  was

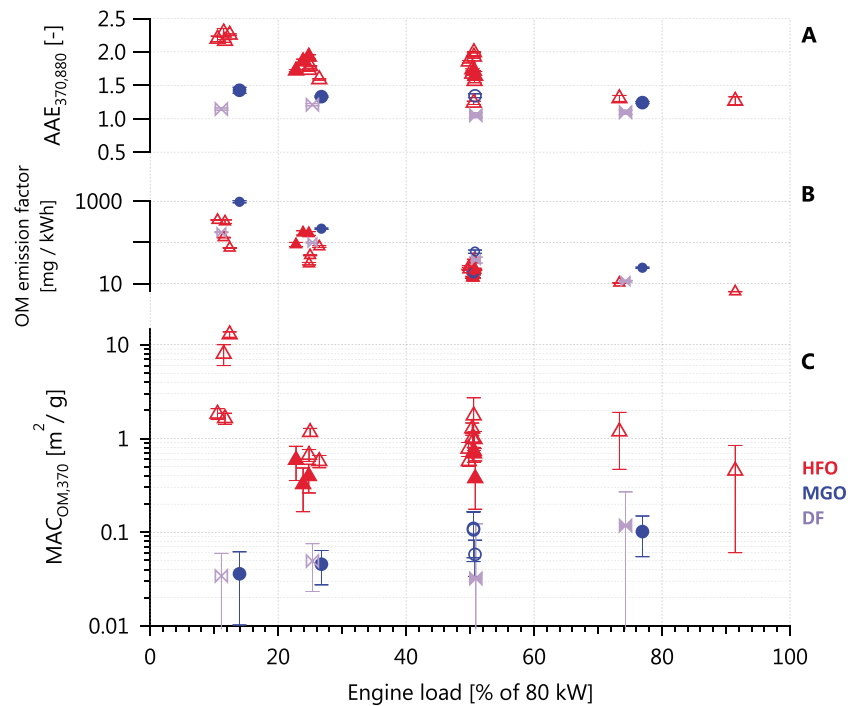


**Figure 7.** (a) AAEs between 370 and 880 nm, (b) OM emission factors, and (c) brC MAC (referencing total OM) plotted against engine load for the three fuels. In (c), open symbols indicate the use of the median rather than the CAPS-PM<sub>s</sub>a-measured AE33 C value. Fewer MAC<sub>OM</sub> data points than  $b_{abn}$  data points are reported due to some missing  $C_{OM}$  measurements. Note that the increase of the MAC at 11% engine load does not correspond to an increase of the OM emission factor. Note also the log scales. AAE = Ångström exponent; HFO = heavy fuel oil; MGO = marine gas oil; DF = diesel fuel; MAC = mass absorption cross section; CAPS PM<sub>s</sub>a = Cavity Attenuation Phase Shift PM SSA monitor; OM = organic PM; brC = brown carbon.

higher than expected. Further work is needed to clarify why this HFO MAC<sub>rBC,780 nm</sub> was higher than previously reported values.

Some difference in MAC<sub>rBC,780 nm</sub> for HFO compared to the distillate fuels may have been anticipated due to the presence of a large rBC mode in HFO PM (section 3.1.1). This was not observed. One may therefore hypothesize that all rBC particles consisted of soot aggregates, since the MAC<sub>rBC,780 nm</sub> of a soot aggregate depends primarily on the size of its monomers (Sorensen, 2001) and not on its overall size. However, as measurements on char particles are lacking in the literature, it is not clear that the MAC<sub>rBC,780 nm</sub> (and other optical properties) of small char particles would be sufficiently different from soot to be seen in Figures 5b and S1. Regardless of the physical interpretation, our data indicate that the anomalous size distribution of HFO PM did not lead to an anomalous MAC<sub>rBC,780 nm</sub>. We note, however, that SP2 measurements were not available for the lowest engine load test points, for which brC absorption appeared to be anomalously high.

### 3.2. Brown Carbon

In this section, we discuss the wavelength dependence and intensive properties of brC. The focus is on HFO PM, since brC was negligible in the other fuels.

We reiterate here that these calculations are numerically independent of the SP2 data discussed in section 3.1.1, as shown in the schematic diagram Figure 2. Uncertainties related to the larger mode of rBC particles measured in HFO PM by SP2 are therefore irrelevant to the following results. In particular, we used only the  $b_{abn,780 nm}$  measured by CAPS PM<sub>s</sub>a and the AAE measured by the AE33 to calculate  $k_{OM}$ . The assumptions are that  $AAE_{BC} = 1$  and that only BC absorbs at  $\lambda > 700$  nm.

#### 3.2.1. Wavelength Dependence of Light Absorption

Figure 6 shows AE33 absorption spectra for all engine test points. The data are normalized to 880 nm to allow different concentrations to be compared. The distillate fuels (DF and MGO) show similar trends and are consistent with an AAE of  $1 \pm 0.1$  down to 470 nm. At 370 nm, there is some evidence of a minor contribution (<20% of  $b_{abn}$  at 370 nm) of brC to light absorption for the distillate fuels.



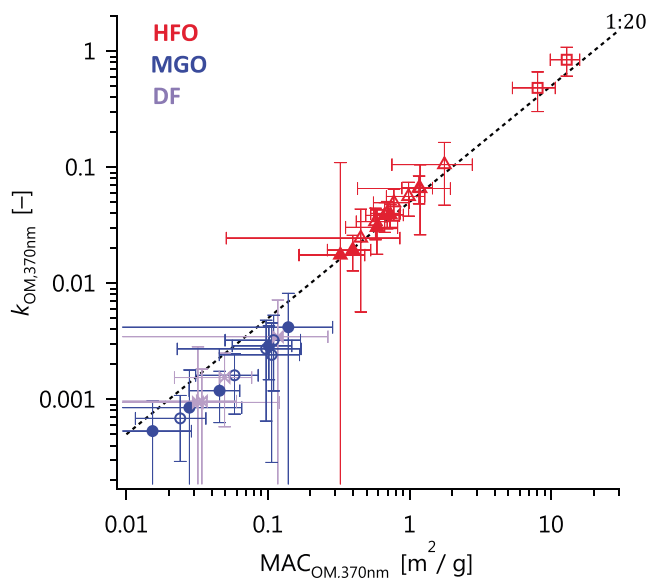


**Figure 8.** Retrieved OM imaginary refractive indices plotted against MAC at 370 nm. The two high-valued outliers (square symbols) represent 11%-load conditions (see Figure 7). The observed good correlation indicates that variability in  $k_{OM}$  was driven by variability in the OM properties (particularly engine conditions) rather than particle size or other Mie model parameters. OM = organic PM; MAC = mass absorption cross section; HFO = heavy fuel oil.

For HFO, the data are generally consistent with an AAE(370–950) of  $1.7 \pm 0.2$ . The shaded region in Figure 6 encompasses this range, showing that this AAE includes the majority of the data points while slightly underpredicting absorption at  $\lambda < 500$  nm. We hypothesized that the scatter in Figure 6 may be related to a varying mass fraction of BC (relative to OM and sulfate) but found this was not the case (Figure S4).

Figure 6 also includes MWA measurements of light absorption of the filter samples. These spectral measurements provide additional confidence in the AE33 data, since the MWA directly measures and corrects for light scattering from the filter sample. The MWA data represent only three HFO filter samples due to limited sample availability but generally corroborate the AE33-measured AAEs.

### 3.2.2. $MAC_{OM,370}$

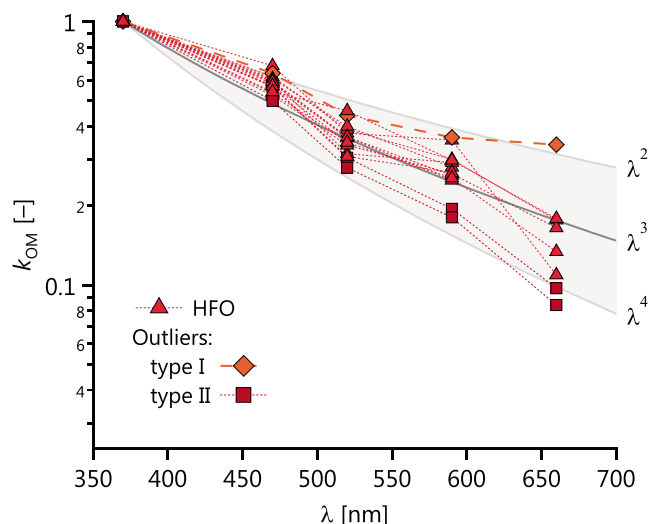
Figure 7c shows brC absorption at 370 nm, per mass of OM ( $MAC_{OM,370}$ ) for all fuels as a function of engine load. For cases in which the median AE33 C value was used, rather than a specifically calibrated C value, the data are shown with open rather than filled symbols. The upper panel, Figure 7a, illustrates the AE33-measured AAEs from which these MACs have been derived.

Figure 7c shows that the  $MAC_{OM,370}$  increased by an order of magnitude at the lowest engine load for HFO. This increase did not correspond to a change in the overall OM emission factor  $EF_{OM}$ , as seen by comparison to Figure 7b, nor to a change in the sampled OM concentrations (not shown). Therefore, this change must be due to a difference in the chemical composition of the OM. (For this reason, we hypothesized that the less-volatile thermal-optical OC fractions would correlate with  $MAC_{OM,370}$  but found that the correlation was poor (section S5).) The relative emission factors of polycyclic aromatic hydrocarbons (PAHs), including oxygenated and nitrogenated PAHs, have been reported to increase at low engine loads by Sippula et al. (2014). Such species have been connected to the chemical composition of the fuel (Rüger et al., 2015; Streibel et al., 2017). The optical properties are thus not adequately described by the lubricating-oil model proposed by Eichler et al. (2017), who only discussed engine emissions at 50% load.

### 3.2.3. Imaginary Refractive Index of OM, $k_{OM,\lambda}$

Based on the measurements described in the previous sections, a Mie model was constructed and fit to the data to obtain the imaginary refractive index of OM for this study, as detailed in section 2.5.

Figures 8 and 9 show the results of the Mie model fits. Figure 8 shows  $k_{OM,370}$  as a function of  $MAC_{OM,370}$ . The two quantities are correlated because the main variations in model inputs were in OM mass concentration and light absorption, rather than particle size or density. Two extreme outliers have a  $k_{OM,370}$  close to unity, which is unusually high. We carefully inspected all input data for these outliers but found no errors. The  $k_{OM,370}$  for DF and MGO was not significantly different from zero.



**Figure 9.** Retrieved imaginary refractive indices as a function of wavelength, normalized to  $k_{OM,370\text{ nm}}$ . Data where  $k_{OM,\lambda} < 0.005$  were omitted due to unreliable data (see error bars in Figure 8). Outlier type I refers to the high outlier at 660 nm; outlier type II refers to the two high- $k_{OM}$  cases shown in Figure 8. The labels  $\lambda^x$  refer to power laws with exponent  $x$ . A power law with  $x$  between  $-2$  and  $-4$  adequately describes the data. OM = organic PM; MAC = mass absorption cross section; HFO = heavy fuel oil; MGO = marine gas oil; DF = diesel fuel.

Figure 9 depicts the wavelength dependence of  $k_{OM}$  by normalizing  $k_{OM,\lambda}$  to  $k_{OM,370}$  for all data. The gray shading and lines show the behavior that would be expected for a  $k_{OM}$  AAE of 2, 3, and 4 (upper line, central line, and lower line). The plot was filtered to only included points where  $k_{OM,\lambda} > 0.005$  before normalization. This threshold is based on the Monte-Carlo-estimated uncertainties shown in Figure 8 and resulted in the exclusion of all MGO and DF data.

Two types of outliers are noticeable in Figure 9. The first, “outlier I,” shows an anomalously slow decrease in  $k_{OM}$  with  $\lambda$ . The reason for this exception was not identified. The second, “outlier II,” corresponds to the two high outliers in Figure 8. The  $k_{OM}$ -versus- $\lambda$  trend for both of these type-II outliers appears reasonable and is similar; compared to the other measurements the slope is more negative than expected. In other words, in addition to having higher absolute  $k_{OM,370}$  these measurements also had a higher ratio  $k_{OM,370}:k_{OM,660}$ , which is consistent with a true chemical difference in the type-II samples.

## 4. Discussion

### 4.1. Expected Differences Between Engines and HFO Samples

In general, the intensive optical properties of marine engine PM may vary between studies. In our present study, we have observed similar optical properties to those observed in the study described by Mueller et al. (2015), as discussed in detail in section S5. Further measurements are required to describe the degree to which engine-to-engine variability may influence these properties.

In addition, differences in fuel composition may influence marine engine PM optical properties. Since the molecular composition of HFO PM has been shown to be comparable with the molecular composition of HFO (Streibel et al., 2017), in a manner depending on engine load (Sippula et al., 2014), we hypothesize that the molecular composition of brC is also related to the molecular composition of the fuel. In support of this hypothesis, we note that Sippula et al. (2014) observed larger mass fractions of PAHs in HFO OM at lower engine loads, similar to our observation of increased  $MAC_{OM}$  at lower engine loads. Those authors suggested that the PAHs in HFO PM represent unburned fuel. This picture is consistent with the nonabsorbing nature of the distillate-fuel PM samples, since neither MGO nor DF contain substantial levels of PAHs.

If PAHs in HFO are a major source of brC in HFO PM, then different engines may produce brC in a similar manner to one another. Thus, the extrapolation of the  $MAC_{OM}$  and  $k_{OM}$  reported herein to other engines may be justified, especially when using the relationship of OC3/OC with  $MAC_{OM,370}$  (Figure S5) to estimate light absorption by brC in HFO PM. However, since variability in the composition of HFO fuel (Stout & Wang, 2016)

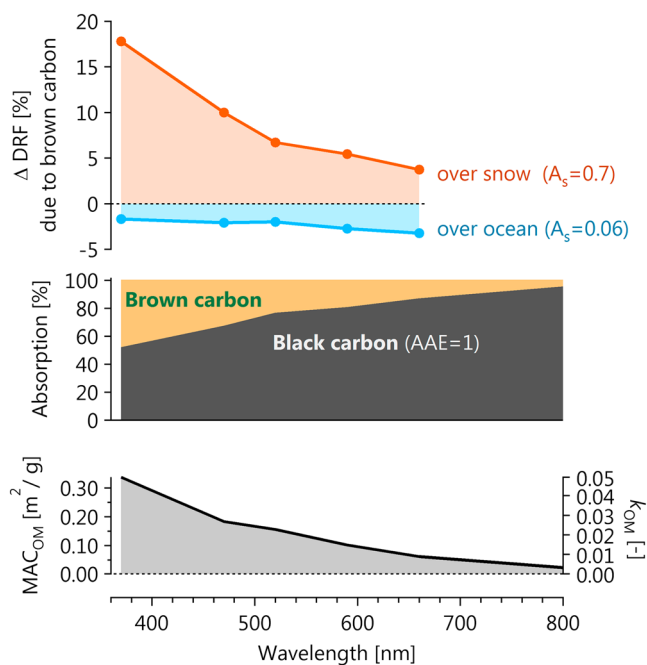


**Figure 10.** Depiction of the importance of brown carbon absorption for a typical case at 50% load. Here brC is defined by the BC + brC approach as excess absorption after subtracting BC absorption via  $AAE_{BC,880\text{ nm}} = 1$ . (top) Percent change in direct radiative forcing due to brown carbon, relative to a reference case of nonabsorbing organics. (middle) Contribution of organics and black carbon to overall absorption. (bottom)  $MAC_{OM}$  and  $k_{OM}$  used for this analysis. MAC = mass absorption cross section; BC = black carbon; brC = brown carbon; AAE = Ångström exponent; OM = organic PM.

may lead to variability in the light-absorbing properties of the emissions, additional studies are warranted to constrain fuel-related variability in  $k_{OM}$  and  $MAC_{OM}$ .

#### 4.2. Summary and Implications of brC/OM Light Absorption

In the following, we summarize the results on brC absorption and provide an illustration of the potential radiative impacts of HFO brC.

The standard operating load for this engine is 50%, although engines frequently operate at lower loads to save fuel or in the presence of ice (Lack & Corbett, 2012). At 50% load, the mean  $k_{OM,370\text{ nm}}$  and corresponding SD were  $0.057 \pm 0.027$  ( $n = 5$ ). At 25% load, the corresponding values were  $0.034 \pm 0.018$  ( $n = 6$ ). Considering the large variabilities, we recommend the combined mean,  $0.045 \pm 0.025$ , for modeling studies. According to Figure 9,  $k_{OM,\lambda}$  may then be estimated as

$$k_{OM,\lambda} = (0.045 \pm 0.025)(\lambda/370\text{ nm})^{-3}, \quad 370\text{ nm} < \lambda < 660\text{ nm} \quad (6)$$

At the commonly used  $\lambda$  of 550 nm, equation (6) gives  $k_{OM,550\text{ nm}} = 0.014 \pm 55\%$ . Compared to the  $k_{OM,550\text{ nm}}$  values summarized by the review of Lu et al. (2015), this is a high value. For example, those authors recommended  $k_{OM,550\text{ nm}} = 0.015 \pm 45\%$  for lignite OM and  $k_{OM,550\text{ nm}} \approx 0.03$  for biomass-combustion OM with 10% BC (a comparable BC fraction to our data). For HFO, Lu et al. (2015) recommended  $k_{OM,550\text{ nm}} = 0.006 \pm 40\%$ , based on the extrapolation of studies of DF emissions to HFO. This is a factor of 2.3 smaller than our measured value. Considering that we measured negligible brC for DF PM, this extrapolation is not valid and future studies should use equation (6) to estimate  $k_{OM}$  for HFO.

The very high OM fraction (approximately 90%) in HFO emissions makes brC light absorption especially important for this aerosol in spite of its  $k_{OM}$  (at 25–50% engine load) falling within the range of previously reported values (for other brC sources). This is demonstrated in Figure 10, where the Simple Forcing Efficiency (Bond & Bergstrom, 2006; Chen & Bond, 2010) has been employed. The figure illustrates the Direct Radiative Forcing (DRF) of a representative ship-exhaust plume over the planet's surface. A wavelength-dependent mass scattering cross section of  $2.3\text{ m}^2/\text{g}$  at 780 nm and scaling exponent of 4 (see supporting information for details)

was used with a backscatter fraction of 0.1. For the 50% load case (inputs shown in lower panel), the figure plots the relative absorption of OM and BC (middle panel) and the estimated change in DRF (upper panel) when including brC absorption. The change in DRF is relative to the base case of nonabsorbing OM (equal OM mass, with  $k_{OM}$  set to zero). Relative humidity effects have been neglected for simplicity. The DRF is highly sensitive to the albedo of the surface below the aerosol; as such, two cases are shown: one for the case of fresh snow or cloud, one for the case of the dark ocean.

Note that OM absorption from HFO at  $\lambda = 660$  nm is  $\sim 20\%$  of the total. At this wavelength, brC absorption may have been expected to have dropped to zero (Laskin et al., 2015): HFO brC clearly absorbs farther into the red than expected. At  $\lambda = 370$  nm, the contribution of brC to the DRF increases to 18% for the over-snow case. Note that we have chosen a conservative example of 50% load and that  $MAC_{OM}$  was much larger at lower loads (Figure 7). The ability of brC absorption to influence the DRF of HFO-exhaust PM, particularly in high-albedo environments like the Arctic, should motivate modeling studies to assess the overall climate effects of HFO brC absorption.

## 5. Conclusions

We used in situ measurements of single-particle black carbon mass (via laser-induced incandescence), in situ aerosol light extinction and scattering coefficients, and filter-based measurements of Ångström absorption exponents, to reach several conclusions on the properties of BC and brC in emissions from an auxiliary-scale research ship engine. One residual fuel (HFO) and two distillate fuels (marine gas oil, MGO, and DF) were used.

Overall, light absorption by OM in DF and MGO exhaust was found to be negligible, whereas absorption by OM in HFO PM was very significant. This result was not surprising considering the near black color of the HFO fuel (diesel is almost transparent) and the molecular similarity between HFO-exhaust OM and the fuel (Sippula et al., 2014; Streibel et al., 2017). In more detail, our conclusions are as follows.

1. Generally, BC was externally mixed from nonrefractory material (sulfates and organics) in the primary emissions. The BC size distribution for DF and MGO was a typical lognormal, whereas for HFO an apparent bimodal lognormal with very large rBC particles was observed.
2. The ratio of 780-nm light absorption coefficient with rBC mass gave a  $MAC_{rBC,780\text{ nm}}$  of  $7.8 \pm 1.8$  m<sup>2</sup>/g from SP2 and in situ absorption measurements for all three fuels.
3. The overall wavelength dependence of absorption ( $370 < \lambda < 950$  nm) for this PM can be generally described by an AAE of  $1.0 \pm 0.1$  for MGO and DF and by an AAE of  $1.7 \pm 0.2$  for HFO.
4. Considering the PM as a mixture of brC and BC with  $AAE_{BC} = 1$  (BC + brC model), only HFO was found to contain significant amounts of brC, with  $MAC_{OM,370\text{ nm}} = 0.4 \pm 0.2$  m<sup>2</sup>/g at typical operating conditions of 50% load. At low engine loads (11%), MACs up to 10 m<sup>2</sup>/g were observed while OM emission factors remained unchanged, indicating a fundamental change in the nature of the absorbing material.
5. Using a measurement-constrained Mie model, we retrieved wavelength-dependent imaginary refractive indices  $k_{OM,\lambda}$  for HFO of 0.032–0.066 (interquartile range). A parameterization was provided for  $k_{OM,\lambda}$  at typical engine operating conditions (equation (6)). The reported  $k_{OM}$  is large compared to previous values reported for open biomass burning (Lu et al., 2015). Due to the high OM fraction in this exhaust ( $\sim 90\%$ ), OM absorption (brC) may contribute up to 50% of total absorption for HFO at 370 nm, and 20% at 660 nm.
6. A simplified calculation showed that accounting for brC in the radiative forcing of HFO PM may enhance the DRF by 18% at 370 nm and 50% load, and much more at lower engine loads. Climate models should therefore include this absorption when estimating the radiative effects of ship exhaust.

Although the emissions and light-absorbing properties of OM may vary between engines, between engine settings, and between HFO samples, our reported  $k_{OM}$  and  $MAC_{OM}$  values provide a significant improvement over previously available data.

### 5.1. Author Contributions

J. C. C. performed the initial data analysis and interpretation. H. C., M. G., I. E. H., G. M., and L. D. contributed significantly to data interpretation. M. Z., J. C. C., and M. G. operated and calibrated the SP2. S. P. and J. C. C. operated and calibrated the CAPS. G. J. operated the AE33 and provided its data, and L. D. analyzed the AE33 raw data. A. A. M., S. P., and J. C. C. operated and calibrated the AMS. J. C. C. performed the APM measurements. J. O. and B. S. planned and oversaw the experiments. A. S. H. P. and R. Z. initiated the study. J. C. C. wrote the manuscript, and all authors contributed to the writing.

## Acknowledgments

We thank Anna Possner for input leading to the Mie model and Jonathan Taylor for the Mie program. We thank also Branka Miljevic, Nivedita Kumar, and the University of Rostock staff for their work and assistance during the measurements. This project, WOOSHI, was funded by the Swiss National Science Foundation (SNSF, project 140590), the German research foundation (DFG, grant Zi 764/5-1), and the Helmholtz Virtual Institute "HICE – Aerosol and Health" (www.hice-vi.eu) via the Helmholtz Association (HGF-INF). J. C. C., M. Z., and M. G. received financial support from the ERC under grant ERC-CoG-615922-BLACARAT. G. M. and L. D. were employed by Aerosol d.o.o., where the Aethalometer AE33 was developed and is being produced. Emission factor and brC properties data are included in the supporting information.

## References

- Abo Riziq, A., Erlick, C., Dinar, E., & Rudich, Y. (2007). Optical properties of absorbing and non-absorbing aerosols retrieved by cavity ring down (CRD) spectroscopy. *Atmospheric Chemistry and Physics*, 7(6), 1523–1536. <https://doi.org/10.5194/acp-7-1523-2007>
- Bahadur, R., Praveen, P. S., Xu, Y., & Ramanathan, V. (2012). Solar absorption by elemental and brown carbon determined from spectral observations. *Proceedings of the National Academy of Sciences of the United States of America*, 109(43), 17,366–17,371. <https://doi.org/10.1073/pnas.1205910109>
- Bond, T. C., & Bergstrom, R. W. (2006). Light absorption by carbonaceous particles: An investigative review. *Aerosol Science and Technology*, 40(1), 27–67. <https://doi.org/10.1080/02786820500421521>
- Buffaloe, G., Lack, D., Williams, E., Coffman, D., Hayden, K., Lerner, B., et al. (2014). Black carbon emissions from in-use ships: A California regional assessment. *Atmospheric Chemistry and Physics*, 14(4), 1881–1896. <https://doi.org/10.5194/acp-14-1881-2014>
- Burtscher, H. (2005). Physical characterization of particulate emissions from diesel engines: A review. *Journal of Aerosol Science*, 36(7), 896–932. <https://doi.org/10.1016/j.jaerosci.2004.12.001>
- Cazorla, A., Bahadur, R., Suski, K., Cahill, J. F., Chand, D., Schmid, B., et al. (2013). Relating aerosol absorption due to soot, organic carbon, and dust to emission sources determined from in-situ chemical measurements. *Atmospheric Chemistry and Physics*, 13(18), 9337–9350. <https://doi.org/10.5194/acp-13-9337-2013>
- Chen, Y., & Bond, T. (2010). Light absorption by organic carbon from wood combustion. *Atmospheric Chemistry and Physics*, 10(4), 1773–1787. <https://doi.org/10.5194/acp-10-1773-2010>
- Chen, Y., Shah, N., Braun, A., Huggins, F. E., & Huffman, G. P. (2005). Electron microscopy investigation of carbonaceous particulate matter generated by combustion of fossil fuels. *Energy & Fuels*, 19(4), 1644–1651. <https://doi.org/10.1021/ef049736y>
- Corbett, J. J., Winebrake, J. J., Green, E. H., Kasibhatla, P., Eyring, V., & Lauer, A. (2007). Mortality from ship emissions: A global assessment. *Environmental Science & Technology*, 41(24), 8512–8518. <https://doi.org/10.1021/es071686z>
- Corbin, J. C., Mensah, A. A., Pieber, S. M., Orasche, J., Michalke, B., Zanatta, M., et al. (2018). Trace metals in soot and PM<sub>2.5</sub> from heavy-fuel-oil combustion in a marine engine. *Environmental Science & Technology*. <https://doi.org/10.1021/acs.est.8b01764>
- DeCarlo, P. F., Kimmel, J. R., Trimborn, A., Northway, M. J., Jayne, J. T., Aiken, A. C., et al. (2006). Field-deployable, high-resolution, time-of-flight aerosol mass spectrometer. *Analytical Chemistry*, 78(24), 8281–8289. <https://doi.org/10.1021/ac061249n>
- Drinovec, L., Močnik, G., Zotter, P., Prévôt, A. S. H., Ruckstuhl, C., Coz, E., et al. (2015). The "dual-spot" aethalometer: An improved measurement of aerosol black carbon with real-time loading compensation. *Atmospheric Measurement Techniques*, 8(5), 1965–1979. <https://doi.org/10.5194/amt-8-1965-2015>
- Eichler, P., Müller, M., Rohmann, C., Stengel, B., Orasche, J., Zimmermann, R., & Wisthaler, A. (2017). Lubricating oil as a major constituent of ship exhaust particles. *Environmental Science and Technology Letters*, 4(2), 54–58. <https://doi.org/10.1021/acs.estlett.6b00488>
- Endresen, Ø. (2003). Emission from international sea transportation and environmental impact. *Journal of Geophysical Research*, 108(D17), 4560. <https://doi.org/10.1029/2002JD002898>
- Eyring, V., Isaksen, I. S., Bernsten, T., Collins, W. J., Corbett, J. J., Endresen, O., et al. (2010). Transport impacts on atmosphere and climate: Shipping. *Atmospheric Environment*, 44(37), 4735–4771. <https://doi.org/10.1016/j.atmosenv.2009.04.059>
- Favez, O., Alfaro, S. C., Sciare, J., Cachier, H., & Abdelwahab, M. M. (2009). Ambient measurements of light-absorption by agricultural waste burning organic aerosols. *Journal of Aerosol Science*, 40(7), 613–620. <https://doi.org/10.1016/j.jaerosci.2009.04.002>
- Fialho, P., Hansen, A., & Honrath, R. (2005). Absorption coefficients by aerosols in remote areas: A new approach to decouple dust and black carbon absorption coefficients using seven-wavelength aethalometer data. *Journal of Aerosol Science*, 36(2), 267–282. <https://doi.org/10.1016/j.jaerosci.2004.09.004>
- Fridell, E., Steen, E., & Peterson, K. (2008). Primary particles in ship emissions. *Atmospheric Environment*, 42(6), 1160–1168. <https://doi.org/10.1016/j.atmosenv.2007.10.042>
- Gao, R. S., Schwarz, J. P., Kelly, K. K., Fahey, D. W., Watts, L. A., Thompson, T. L., et al. (2007). A novel method for estimating light-scattering properties of soot aerosols using a modified single-particle soot photometer. *Aerosol Science and Technology*, 41(2), 125–135. <https://doi.org/10.1080/02786820601118398>
- Grenfell, T. C., Doherty, S. J., Clarke, A. D., & Warren, S. G. (2011). Light absorption from particulate impurities in snow and ice determined by spectrophotometric analysis of filters. *Applied Optics*, 50(14), 2037. <https://doi.org/10.1364/ao.50.002037>
- Huang, X.-F., Gao, R. S., Schwarz, J. P., He, L.-Y., Fahey, D. W., Watts, L. A., et al. (2011). Black carbon measurements in the Pearl River Delta region of China. *Journal of Geophysical Research*, 116, D12208. <https://doi.org/10.1029/2010JD014933>
- Huang, Y., Zhao, R., Jiang, J., & Zhu, K.-Y. (2012). Scattering and absorptive characteristics of a cenosphere. *International Journal of Thermal Sciences*, 57, 63–70. <https://doi.org/10.1016/j.ijthermalsci.2012.01.019>
- Jimenez, J. L., Canagaratna, M. R., Drewnick, F., Allan, J. D., Alfarra, M. R., Middlebrook, A. M., et al. (2016). Comment on "the effects of molecular weight and thermal decomposition on the sensitivity of a thermal desorption aerosol mass spectrometer". *Aerosol Science and Technology*, 50(9), i–xv. <https://doi.org/10.1080/02786826.2016.1205728>
- Kasper, A., Aufdenblatten, S., Forss, A., Mohr, M., & Burtscher, H. (2007). Particulate emissions from a low-speed marine diesel engine. *Aerosol Science and Technology*, 41(1), 24–32. <https://doi.org/10.1080/02786820601055392>
- Kondo, Y., Sahu, L., Moteki, N., Khan, F., Takegawa, N., Liu, X., et al. (2011). Consistency and traceability of black carbon measurements made by laser-induced incandescence, thermal-optical transmittance, and filter-based photo-absorption techniques. *Aerosol Science and Technology*, 45(2), 295–312. <https://doi.org/10.1080/02786826.2010.533215>
- Kulkarni, G., Pekour, M., Afchine, A., Murphy, D. M., & Cziczo, D. J. (2011). Comparison of experimental and numerical studies of the performance characteristics of a pumped counterflow virtual impactor. *Aerosol Science and Technology*, 45(3), 382–392. <https://doi.org/10.1080/02786826.2010.539291>
- Kuwata, M., Zorn, S. R., & Martin, S. T. (2012). Using elemental ratios to predict the density of organic material composed of carbon, hydrogen, and oxygen. *Environmental Science & Technology*, 46(2), 787–794. <https://doi.org/10.1021/es202525q>
- Laborde, M., Crippa, M., Tritscher, T., Jurányi, Z., DeCarlo, P., Temime-Roussel, B., et al. (2012). Black carbon physical properties and mixing state in the European megacity Paris. *Atmospheric Chemistry and Physics*, 12, 25,121–25,180. <https://doi.org/10.5194/acp-12-25121-2012>
- Laborde, M., Mertes, P., Zieger, P., Dommen, J., Baltensperger, U., & Gysel, M. (2012). Sensitivity of the single particle soot photometer to different black carbon types. *Atmospheric Measurement Techniques*, 5, 1031–1043. <https://doi.org/10.5194/amt-5-1031-2012>
- Laborde, M., Schnaiter, M., Linke, C., Saathoff, H., Naumann, K., Möhler, O., et al. (2012). Single particle soot photometer intercomparison at the AIDA chamber. *Atmospheric Measurement Techniques*, 5, 3077–3097. <https://doi.org/10.5194/amt-5-3077-2012>
- Lack, D. A., & Cappa, C. D. (2010). Impact of brown and clear carbon on light absorption enhancement, single scatter albedo and absorption wavelength dependence of black carbon. *Atmospheric Chemistry and Physics*, 10(9), 4207–4220. <https://doi.org/10.5194/acp-10-4207-2010>



- Lack, D. A., & Corbett, J. J. (2012). Black carbon from ships: A review of the effects of ship speed, fuel quality and exhaust gas scrubbing. *Atmospheric Chemistry and Physics*, 12(9), 3985–4000. <https://doi.org/10.5194/acp-12-3985-2012>
- Lack, D. A., Corbett, J. J., Onasch, T., Lerner, B., Massoli, P., Quinn, P. K., et al. (2009). Particulate emissions from commercial shipping: Chemical, physical, and optical properties. *Journal of Geophysical Research*, 114, D00F04. <https://doi.org/10.1029/2008JD011300>
- Lack, D., & Langridge, J. (2013). On the attribution of black and brown carbon light absorption using the Ångström exponent. *Atmospheric Chemistry and Physics*, 13(20), 10,535–10,543. <https://doi.org/10.5194/acp-13-10535-2013>
- Laskin, A., Laskin, J., & Nizkorodov, S. A. (2015). Chemistry of atmospheric brown carbon. *Chemical Reviews*, 115(10), 4335–4382. <https://doi.org/10.1021/cr5006167>
- Lauer, A., Eyring, V., Hendricks, J., Jöckel, P., & Lohmann, U. (2007). Global model simulations of the impact of ocean-going ships on aerosols, clouds, and the radiation budget. *Atmospheric Chemistry and Physics*, 7(19), 5061–5079. <https://doi.org/10.5194/acp-7-5061-2007>
- Linak, W. P., Miller, C. A., & Wendt, J. O. (2000). Fine particle emissions from residual fuel oil combustion: Characterization and mechanisms of formation. *Proceedings of the Combustion Institute*, 28(2), 2651–2658. [https://doi.org/10.1016/S0082-0784\(00\)80684-0](https://doi.org/10.1016/S0082-0784(00)80684-0)
- Lindstad, H., Eskeland, G. S., Psarftis, H., Sandaa, I., & Strømman, A. H. (2015). Maritime shipping and emissions: A three-layered, damage-based approach. *Ocean Engineering*, 110, 94–101. <https://doi.org/10.1016/j.oceaneng.2015.09.029>
- Liu, P. S. K., Deng, R., Smith, K. A., Williams, L. R., Jayne, J. T., Canagaratna, M. R., et al. (2007). Transmission efficiency of an aerodynamic focusing lens system: Comparison of model calculations and laboratory measurements for the aerodyne aerosol mass spectrometer. *Aerosol Science and Technology*, 41(8), 721–733. <https://doi.org/10.1080/02786820701422278>
- Liu, D., Taylor, J. W., Young, D. E., Flynn, M. J., Coe, H., & Allan, J. D. (2015). The effect of complex black carbon microphysics on the determination of the optical properties of brown carbon. *Geophysical Research Letters*, 42, 613–619. <https://doi.org/10.1002/2014GL02443>
- Liu, D., Whitehead, J., Alfarra, M. R., Reyes-Villegas, E., Spracklen, D. V., Reddington, C. L., et al. (2017). Black-carbon absorption enhancement in the atmosphere determined by particle mixing state. *Nature Geoscience*, 10(3), 184–188. <https://doi.org/10.1038/ngeo2901>
- Lobo, P., Durdina, L., Smallwood, G. J., Rindlisbacher, T., Siegerist, F., Black, E. A., et al. (2015). Measurement of aircraft engine non-volatile pm emissions: Results of the aviation-particle regulatory instrument demonstration experiment (A-PRIDE) 4 campaign. *Aerosol Science and Technology*, 49, 472–484. <https://doi.org/10.1080/02786826.2015.1047012>
- Lu, Z., Streets, D. G., Winijkul, E., Yan, F., Chen, Y., Bond, T. C., et al. (2015). Light absorption properties and radiative effects of primary organic aerosol emissions. *Environmental Science & Technology*, 49(8), 4868–4877. <https://doi.org/10.1021/acs.est.5b00211>
- Lyyränen, J., Jokiniemi, J., Kauppinen, E. I., & Joutsensaari, J. (1999). Aerosol characterisation in medium-speed diesel engines operating with heavy fuel oils. *Journal of Aerosol Science*, 30(6), 771–784. [https://doi.org/10.1016/S0021-8502\(98\)00763-0](https://doi.org/10.1016/S0021-8502(98)00763-0)
- Marelle, L., Thomas, J. L., Raut, J.-C., Law, K. S., Jalkanen, J.-P., Johansson, L., et al. (2016). Air quality and radiative impacts of arctic shipping emissions in the summertime in northern norway: From the local to the regional scale. *Atmospheric Chemistry and Physics*, 16(4), 2359–2379. <https://doi.org/10.5194/acp-16-2359-2016>
- Massabò, D., Bernardoni, V., Bove, M., Brunengo, A., Cuccia, E., Piazzalunga, A., et al. (2013). A multi-wavelength optical set-up for the characterization of carbonaceous particulate matter. *Journal of Aerosol Science*, 60, 34–46. <https://doi.org/10.1016/j.jaerosci.2013.02.006>
- Massabò, D., Caponi, L., Bernardoni, V., Bove, M., Brotto, P., Calzolari, G., et al. (2015). Multi-wavelength optical determination of black and brown carbon in atmospheric aerosols. *Atmospheric Environment*, 108, 1–12. <https://doi.org/10.1016/j.atmosenv.2015.02.058>
- Moteki, N., & Kondo, Y. (2007). Effects of mixing state on black carbon measurements by laser-induced incandescence. *Aerosol Science and Technology*, 41(4), 398–417. <https://doi.org/10.1080/02786820701199728>
- Moteki, N., Kondo, Y., & Nakamura, S. (2010). Method to measure refractive indices of small nonspherical particles: Application to black carbon particles. *Journal of Aerosol Science*, 41(5), 513–521. <https://doi.org/10.1016/j.jaerosci.2010.02.013>
- Mueller, L., Jakobi, G., Czech, H., Stengel, B., Orasche, J., Arteaga-Salas, J. M., et al. (2015). Characteristics and temporal evolution of particulate emissions from a ship diesel engine. *Applied Energy*, 155, 204–217. <https://doi.org/10.1016/j.apenergy.2015.05.115>
- Mullins, O. C. (2010). The modified Yen model. *Energy & Fuels*, 24(4), 2179–2207. <https://doi.org/10.1021/ef900975e>
- Oeder, S., Kanashova, T., Sippula, O., Sapcaric, S. C., Streibel, T., Arteaga-Salas, J. M., et al. (2015). Particulate matter from both heavy fuel oil and diesel fuel shipping emissions show strong biological effects on human lung cells at realistic and comparable in vitro exposure conditions. *PLoS One*, 10(6), e0126536. <https://doi.org/10.1371/journal.pone.0126536>
- Onasch, T. B., Massoli, P., Kebabian, P. L., Hills, F. B., Bacon, F. W., & Freedman, A. (2015). Single scattering albedo monitor for airborne particulates. *Aerosol Science and Technology*, 49(4), 267–279. <https://doi.org/10.1080/02786826.2015.1022248>
- Petzold, A., Ogren, J., Fiebig, M., Laj, P., Li, S.-M., Baltensperger, U., et al. (2013). Recommendations for the interpretation of “black carbon” measurements. *Atmospheric Chemistry and Physics*, 13(16), 8365–8379. <https://doi.org/10.5194/acp-13-8365-2013>
- Pokhrel, R. P., Beamesderfer, E. R., Wagner, N. L., Langridge, J. M., Lack, D. A., Jayarathne, T., et al. (2017). Relative importance of black carbon, brown carbon, and absorption enhancement from clear coatings in biomass burning emissions. *Atmospheric Chemistry and Physics*, 17(8), 5063–5078. <https://doi.org/10.5194/acp-17-5063-2017>
- Popovicheva, O., Kireeva, E., Shonija, N., Zubareva, N., Persiantseva, N., Tishkova, V., et al. (2009). Ship particulate pollutants: Characterization in terms of environmental implication. *Journal of Environmental Monitoring*, 11(11), 2077–2086. <https://doi.org/10.1039/B908180A>
- Price, D. J., Chen, C.-L., Russell, L. M., Lamjiri, M. A., Betha, R., Sanchez, K., et al. (2016). More unsaturated, cooking-type hydrocarbon-like organic aerosol particle emissions from renewable diesel compared to ultra low sulfur diesel in at-sea operations of a research vessel. *Aerosol Science and Technology*, 51(2), 135–146. <https://doi.org/10.1080/02786826.2016.1238033>
- Rüger, C. P., Sklorz, M., Schwemer, T., & Zimmermann, R. (2015). Characterisation of ship diesel primary particulate matter at the molecular level by means of ultra-high-resolution mass spectrometry coupled to laser desorption ionisation–comparison of feed fuel, filter extracts and direct particle measurements. *Analytical and Bioanalytical Chemistry*, 407(20), 5923–5937. <https://doi.org/10.1007/s00216-014-8408-1>
- Saleh, R., Adams, P. J., Donahue, N. M., & Robinson, A. L. (2016). The interplay between assumed morphology and the direct radiative effect of light-absorbing organic aerosol. *Geophysical Research Letters*, 43, 8735–8743. <https://doi.org/10.1002/2016GL069786>
- Sandradewi, J., Prévôt, A. S., Szidat, S., Perron, N., Alfarra, M. R., Lanz, V. A., et al. (2008). Using aerosol light absorption measurements for the quantitative determination of wood burning and traffic emission contributions to particulate matter. *Environmental Science & Technology*, 42(9), 3316–3323. <https://doi.org/10.1021/es702253m>
- Schwarz, J. P., Gao, R. S., Fahey, D. W., Thomson, D. S., Watts, L. A., Wilson, J. C., et al. (2006). Single-particle measurements of midlatitude black carbon and light-scattering aerosols from the boundary layer to the lower stratosphere. *Journal of Geophysical Research*, 111, D16207. <https://doi.org/10.1029/2006JD007076>
- Schwarz, J. P., Gao, R. S., Spackman, J. R., Watts, L. A., Thomson, D. S., Fahey, D. W., et al. (2008). Measurement of the mixing state, mass, and optical size of individual black carbon particles in urban and biomass burning emissions. *Geophysical Research Letters*, 35, L13810. <https://doi.org/10.1029/2008GL033968>



- Sedlacek, A. J., Lewis, E. R., Onasch, T. B., Lambe, A. T., & Davidovits, P. (2015). Investigation of refractory black carbon-containing particle morphologies using the single-particle soot photometer (SP2). *Aerosol Science and Technology*, *49*(10), 872–885. <https://doi.org/10.1080/02786826.2015.1074978>
- Seinfeld, J. H., & Pandis, S. N. (2012). *Atmospheric chemistry and physics: From air pollution to climate change*. Hoboken, NJ: John Wiley.
- Sippula, O., Stengel, B., Sklorz, M., Streibel, T., Rabe, R., Orasche, J., et al. (2014). Particle emissions from a marine engine: Chemical composition and aromatic emission profiles under various operating conditions. *Environmental Science & Technology*, *48*, 11,721–11,729. <https://doi.org/10.1021/es502484z>, PMID: 25202837.
- Slowik, J. G., Cross, E. S., Han, J.-H., Davidovits, P., Onasch, T. B., Jayne, J. T., et al. (2007). An inter-comparison of instruments measuring black carbon content of soot particles. *Aerosol Science and Technology*, *41*(3), 295–314. <https://doi.org/10.1080/02786820701197078>
- Sorensen, C. (2001). Light scattering by fractal aggregates: A review. *Aerosol Science and Technology*, *35*(2), 648–687. <https://doi.org/10.1080/02786820117868>
- Sorensen, C. (2011). The mobility of fractal aggregates: A review. *Aerosol Science and Technology*, *45*(7), 765–779. <https://doi.org/10.1080/02786826.2011.560909>
- Stephens, M., Turner, N., & Sandberg, J. (2003). Particle identification by laser-induced incandescence in a solid-state laser cavity. *Applied Optics*, *42*(19), 3726–3736. <https://doi.org/10.1364/AO.42.003726>
- Stout, S., & Wang, Z. (2016). *Standard handbook oil spill environmental forensics: Fingerprinting and source identification*. London, UK: Academic Press.
- Streibel, T., Schnelle-Kreis, J., Czech, H., Harndorf, H., Jakobi, G., Jokiniemi, J., et al. (2017). Aerosol emissions of a ship diesel engine operated with diesel fuel or heavy fuel oil. *Environmental Science and Pollution Research*, *24*, 10,976–10,991. <https://doi.org/10.1007/s11356-016-6724-z>
- Taylor, J., Allan, J., Liu, D., Flynn, M., Weber, R., Zhang, X., et al. (2015). Assessment of the sensitivity of core/shell parameters derived using the single-particle soot photometer to density and refractive index. *Atmospheric Measurement Techniques*, *8*(4), 1701–1718. <https://doi.org/10.5194/amt-8-1701-2015>
- Unger, N., Bond, T. C., Wang, J. S., Koch, D. M., Menon, S., Shindell, D. T., & Bauer, S. (2010). Attribution of climate forcing to economic sectors. *Proceedings of the National Academy of Sciences of the United States of America*, *107*(8), 3382–3387. <https://doi.org/10.1073/pnas.0906548107>
- Wang, Q., Huang, R.-J., Zhao, Z., Cao, J., Ni, H., Tie, X., et al. (2016). Physicochemical characteristics of black carbon aerosol and its radiative impact in a polluted urban area of China. *Journal of Geophysical Research: Atmospheres*, *121*, 12,505–12,519. <https://doi.org/10.1002/2016JD024748>
- Wu, Y., Wang, X., Tao, J., Huang, R., Tian, P., Cao, J., et al. (2017). Size distribution and source of black carbon aerosol in urban Beijing during winter haze episodes. *Atmospheric Chemistry and Physics*, *17*(12), 7965–7975. <https://doi.org/10.5194/acp-17-7965-2017>
- Yuan, J.-F., Huang, X.-F., Cao, L.-M., Cui, J., Zhu, Q., Huang, C.-N., et al. (2016). Light absorption of brown carbon aerosol in the RRD region of China. *Atmospheric Chemistry and Physics*, *16*(3), 1433–1443. <https://doi.org/10.5194/acp-16-1433-2016>
- Zieger, P., Väisänen, O., Corbin, J. C., Partridge, D. G., Bastelberger, S., Mousavi-Fard, M., & Rosati, B. (2017). Revising the hygroscopicity of inorganic sea salt particles. *Nature Communications*, *8*, 15883. <https://doi.org/10.1038/ncomms15883>
- Zimmerman, N., Jeong, C.-H., Wang, J. M., Ramos, M., Wallace, J. S., & Evans, G. J. (2015). A source-independent empirical correction procedure for the fast mobility and engine exhaust particle sizers. *Atmospheric Environment*, *100*, 178–184. <https://doi.org/10.1016/j.atmosenv.2014.10.054>
- Zotter, P., Herich, H., Gysel, M., El-Haddad, I., Zhang, Y., Močnik, G., et al. (2017). Evaluation of the absorption Ångström exponents for traffic and wood burning in the aethalometer-based source apportionment using radiocarbon measurements of ambient aerosol. *Atmospheric Chemistry and Physics*, *17*(6), 4229–4249. <https://doi.org/10.5194/acp-17-4229-2017>